Inorganic Chemistry

Article

pubs.acs.org/IC

Ruthenium, Rhodium, Osmium, and Iridium Complexes of Osazones (Osazones = Bis-Arylhydrazones of Glyoxal): Radical versus Nonradical States

Sarat Chandra Patra,[†] Thomas Weyhermüller,[‡] and Prasanta Ghosh*[,†]

[†]Department of Chemistry, R. K. Mission Residential College, Narendrapur, Kolkata 103, West Bengal, India

[‡]Max-Planck Institute for Chemical Energy Conversion, Stiftstrasse 34-36, 45470 Mülheim an der Ruhr, Germany

Supporting Information

ABSTRACT: Phenyl osazone ($L^{NHPh}H_2$), phenyl osazone anion radical ($L^{NHPh}H_2^{\bullet-}$), benzoyl osazone ($L^{NHCOPh}H_2$), benzoyl osazone anion radical ($L^{NHCOPh}H_2^{\bullet-}$), benzoyl osazone monoanion ($L^{NCOPh}HMe^{-}$), and anilido osazone ($L^{NHCONHPh}HMe$) complexes of ruthenium, osmium, rhodium, and iridium of the types *trans*-[$Os(L^{NHPh}H_2)(PPh_3)_2Br_2$] (**3**), *trans*-[$Ir(L^{NHPh}H_2^{\bullet-})(PPh_3)_2Cl_2$] (**4**), *trans*-[$Ru(L^{NHCOPh}H_2)(PPh_3)_2Cl_2$] (**5**), *trans*-[$Os(L^{NHCOPh}H_2)(PPh_3)_2Br_2$] (**6**), *trans*-[$Rh(L^{NHCOPh}H_2^{\bullet-})(PPh_3)_2Cl_2$] (**7**), *trans*-[$Rh(L^{NHCOPh}HMe^{-})(PPh_3)_2Cl]PF_6$ ([**8**]PF_6), and *trans*-[$Ru(L^{NHCONHPh}HMe)(PPh_3)_2Cl]Cl$ ([**9**]Cl) have been isolated and compared (osazones = bis-arylhydrazones of glyoxal). The complexes have been characterized by elemental analyses and IR, mass, and ^1H NMR spectra; in addition, single-crystal X-ray structure determinations of **5**, **6**, [**8**]PF_6, and [**9**]Cl have been carried out. EPR spectra of **4** and **7** reveal that in the solid state they are osazone anion radical complexes (**4**, g_{av} = 1.989; **7**, 2.028 (Δg = 0.103)), while in solution the contribution of the M(II) ions is greater (**4**, g_{av} = 2.052 (Δg = 0.189); **7**, g_{av} = 2.102 (Δg = 0.238)). Mulliken spin densities on $L^{NHPh}H_2$ and $L^{NHCOPh}H_2$ obtained from unrestricted density functional theory (DFT) calculations on *trans*-[$Ir(L^{NHPh}H_2)(PMe_3)_2Cl_2$] ($\mathbf{4}^{Me}$) and *trans*-[$Rh(L^{NHCOPh}H_2)(PMe_3)_2Cl_2$] ($\mathbf{7}^{Me}$) in the gas phase with doublet spin states authenticated the existence of $L^{NHPh}H_2^{\bullet-}$ and $L^{NHCOPh}H_2^{\bullet-}$ anion radicals in **4** and **7** coordinated to iridium(III) and rhodium(III) ions. DFT calculations on *trans*-[$Os(L^{NHPh}H_2)(PMe_3)_2Br_2$] ($\mathbf{3}^{Me}$), *trans*-[$Os(L^{NHCOPh}H_2)(PMe_3)_2Br_2$] ($\mathbf{6}^{Me}$), and *trans*-[$Ru(L^{NHCONHPh}HMe^{-})(PMe_3)_2Cl$] $[\mathbf{9}^{Me}]^+$ with singlet spin states established that the closed-shell singlet state (CSS) solutions of **3**, **5**, **6**, and [**9**]Cl are stable. The lower value of M^{III}/M^{II} reduction potentials and lower energy absorption bands corroborate the higher extent of mixing of d orbitals with the π^* orbital in the case of **3** and **6**. Time-dependent (TD) DFT calculations elucidated the MLCT as the origin of the lower energy absorption bands of **3**, **5**, and **6** and $\pi \rightarrow \pi^*$ as the origin of transitions in **4** and **7**.

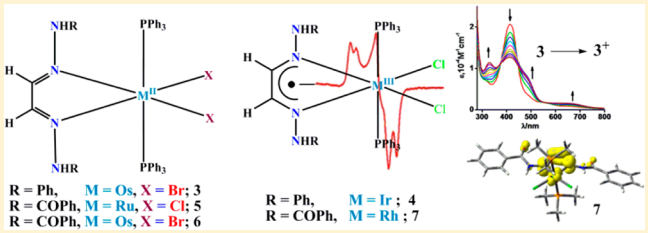

INTRODUCTION

Electronic structures of the α-diimine complexes are complex. Coordinated α-diimine fragments are redox active and can exist in three different electronic states. The three defined electronic states of a coordinated diimine are neutral diimine ($L^RR'_2$),[1] monoanionic diimine anion radical ($L^RR'_2{}^{\bullet-}$),[2] and dianionic diimide,[3] as illustrated in Scheme 1. The states have been well-defined by the bond parameters, spectra, redox potentials, and quantum chemical calculations.[1−3]

Other than these three states, the bond parameters of the diimine fragment in many cases are significantly perturbed due to the back-bonding effect. Strong interactions between the unoccupied π^* ($\pi^* = \pi_{diimine}{}^*$) and the filled metal d orbitals defined as the back-bonding result in the delocalization of the metal electron density over the conjugated diimine fragment,[1] which is reducible at lower potential. In such cases, the extent of deformation of the coordinated $L^RR'_2$ unit is expected to depend on the substituents R and R′ and the types of metal d orbitals involved. Density functional theory (DFT) calculations correlating the bond parameters of the diimine fragment, with lower energy metal to ligand charge transfer (MLCT), in conjunction with the redox potential data help us to elucidate these electronic states satisfactorily.

Osazones are a class of organic compounds that provide stable diimine fragments with a variety of substituents.

Scheme 1

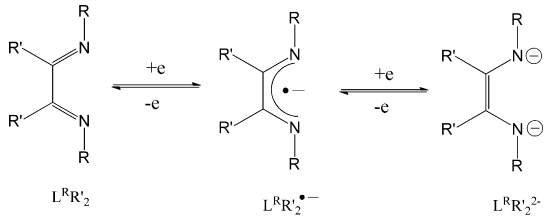

Received: September 3, 2013
Published: February 12, 2014

   dx.doi.org/10.1021/ic4022432 | *Inorg. Chem.* 2014, 53, 2427−2440

Chart 1

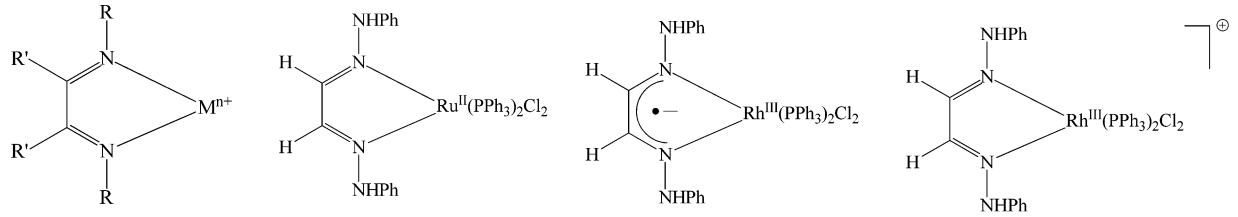

Chart 2

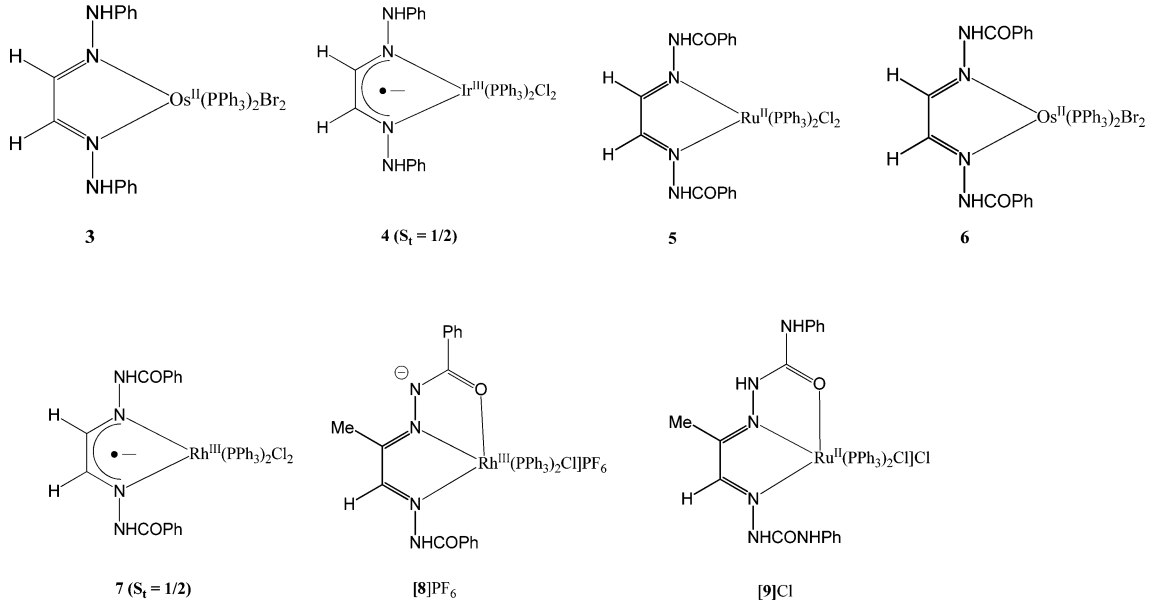

Moreover, π^* of phenyl osazone ($L^{NHPh}H_2$), with lower energy, is a better π acceptor than π^* of a similar type of phenyl diimine ligand (e.g, $E_{\pi^*}(L^{NHPh}H_2) = -2.613$ eV; $E_{\pi^*}(L^{Ph}H_2) = -1.421$ eV; vide infra) ($L^{NHPh}H_2$ = glyoxalbis(*N*-phenyl)-osazone).[4] However, transition-metal osazone complexes have not been explored well. In this article, the issue is addressed, isolating and elucidating the molecular and electronic structures of ruthenium, rhodium, osmium, and iridium complexes of phenyl osazone ($L^{NHPh}H_2$), benzoyl osazones ($L^{NHCOPh}HR'$; R′ = H, Me), and anilido osazone ($L^{NHCONHPh}HMe$) ($L^{NHCOPh}H_2$ = glyoxalbis(*N*-benzoyl)osazone, $L^{NHCOPh}HMe$ = methylglyoxalbis(*N*-benzoyl)osazone, and $L^{NHCONHPh}HMe$ = methylglyoxalbis(*N*-anilido)osazone).

The important phenyl osazone complexes reported so far are *trans*-[$Ru(L^{NHPh}H_2)(PPh_3)_2Cl_2$] (**1**),[5] *trans*-[$Rh^{III}(L^{NHPh}H_2^{\bullet-})(PPh_3)_2Cl_2$] (**2**),[6] and *trans*-[$Rh^{III}(L^{NHPh}H_2)(PPh_3)_2Cl_2]I_3$ [**2**]I_3[6] with 4d metal ions, as depicted in Chart 1. **2** incorporates the phenyl osazone anion radical ($L^{NHPh}H_2^{\bullet-}$) coordinated to a rhodium(III) ion, while the electronic state of the [$Ru(L^{NHPh}H_2)$] unit of **1** is complex. Single-crystal X-ray bond parameters and molecular orbital analyses by density functional theory (DFT) calculations on **1** established a strong interaction between π^* and metal d orbitals shifting the metal electron to the diimine fragment to the extent of 0.3e, distorting the diimine fragment notably. These two reports determined that the $L^{NHPh}H_2$ is redox noninnocent.

To substantiate the osazone diimine chemistry, in addition to the phenyl osazone, the coordination chemistry of benzoyl and anilido osazones with 4d and 5d metal ions has also been explored. The energies of the π^* of the phenyl and the benzoyl osazones are different. In the gas phase, $E_{\pi^*}(L^{NHCOPh}H_2)$ (−1.82 eV) is less than $E_{\pi^*}(L^{Ph}H_2)$ (−1.421 eV) but higher than $E_{\pi^*}(L^{NHPh}H_2)$ (−2.613 eV). On the other hand, benzoyl ($L^{NHCOPh}HR'$) and anilido osazones ($L^{NHCONHPh}HMe$) exhibit binding modes those are different from that of the phenyl osazone ($L^{NHPh}H_2$). In comparison to $L^{NHPh}H_2$, $L^{NHCOPh}HR'$ and $L^{NHCONHPh}HMe$ liberate a proton easily to form a monoanionic chelate. In this work, new coordination complexes of the types *trans*-[$Os^{II}(L^{NHPh}H_2)(PPh_3)_2Br_2$] (**3**), *trans*-[$Ir^{III}(L^{NHPh}H_2^{\bullet-})(PPh_3)_2Cl_2$] (**4**), *trans*-[$Ru^{II}(L^{NHCOPh}H_2)(PPh_3)_2Cl_2$] (**5**), *trans*-[$Os^{II}(L^{NHCOPh}H_2)(PPh_3)_2Br_2$] (**6**), *trans*-[$Rh^{III}(L^{NHCOPh}H_2^{\bullet-})(PPh_3)_2Cl_2$] (**7**), *trans*-[$Rh^{III}(L^{NHCOPh}HMe^{-})(PPh_3)_2Cl]PF_6$ ([**8**]PF_6), and *trans*-[$Ru^{II}(L^{NHCONHPh}HMe)(PPh_3)_2Cl]Cl$ ([**9**]Cl), which are illustrated in Chart 2, were successfully isolated. Single-crystal X-ray structures, spectra, redox potentials, and DFT calculations have authenticated the molecular and electronic structures of **3**−**7**, [**8**]PF_6, and [**9**]Cl. Electronic states of the osazone diimine fragments of these complexes are correlated with the redox potential data and spectral features.

EXPERIMENTAL SECTION

Physical Measurements. Reagents or analytical grade materials were obtained from commercial suppliers and used without further purification. Spectroscopic grade solvents were used for spectroscopic and electrochemical measurements. The C, H, and N contents of the

dx.doi.org/10.1021/ic4022432 | Inorg. Chem. 2014, 53, 2427−2440

compounds were obtained from a Perkin-Elmer 2400 Series II elemental analyzer. Infrared spectra of the samples were measured from 4000 to 400 cm^{-1} with KBr pellets at room temperature on a Perkin-Elmer Spectrum RX 1 FT-IR dpectrophotometer. ^1H NMR spectra in DMSO-d_6 and $CDCl_3$ solvents were obtained on a Bruker DPX 300 MHz spectrometer. ESI mass spectra were recorded on a micro mass Q-TOF mass spectrometer. Electronic absorption spectra in solution at 298 K were obtained on a Perkin-Elmer Lambda 25 spectrophotometer in the range 1100−200 nm. The X-band electron paramagnetic resonance (EPR) spectra at 298 and 130 K were measured on a Magnettech GmbH MiniScope MS400 spectrometer (equipped with temperature controller TC H03), where the microwave frequency was measured with an FC400 frequency counter. Magnetic susceptibilities at 298 K were measured on a Sherwood Magnetic Susceptibility Balance. The electro analytical instrument BASi Epsilon-EC was used for cyclic voltammetric experiments and spectroelectrochemistry measurements. All of the EPR spectra simulations were made by Easy Spin software.

Syntheses. *Glyoxalbis(N-phenyl)osazone ($L^{NHPh}H_2$).* This compound was prepared by the reported procedure.[5]

Glyoxalbis(N-benzoyl)osazone ($L^{NHCOPh}H_2$). To a solution of benzohydrazide (1.36 g, 10 mmol) in methanol (20 mL) was added glyoxal (0.29 g, 5 mmol), and the resulting mixture was stirred for 15 min at 298 K. A white solid separated out, which was filtered and dried in air. Yield: 1.2 g (∼82%). ESI (positive ion)-MS in CH_3OH: m/z 316.95 for $[M + Na]^+$. ^1H NMR (DMSO-d_6, 300 MHz): δ (ppm) 9.76 (s, 2H, NH), 8.17 (s, 2H, =CHCH=), 7.89 (d, 2H, Ph), 7.81 (d, 2H, Ph), 7.57 (m, 3H, Ph), 7.46 (m, 3H, Ph). Anal. Calcd for $C_{16}H_{14}N_4O_2$: C, 65.30; H, 4.79; N, 19.04. Found: C, 64.33; H, 4.69; N, 18.71. IR/cm^{-1} (KBr): ν 3229 (s), 3048 (m), 1658 (vs), 1578 (s), 1309 (s), 1276 (s), 1144 (s), 1051 (s), 965 (s), 907 (s).

Methylglyoxalbis(N-benzoyl)osazone ($L^{NHCOPh}HMe$). To a solution of benzohydrazide (1.36 g, 10 mmol) in methanol (20 mL) was added methylglyoxal (0.36 g, 5 mmol), and the resulting mixture was stirred for 15 min at 298 K. A white solid separated out, which was filtered and dried in air. Yield: 1.3 g (84.41%). ESI (positive ion)-MS in CH_3OH: m/z 309.01 for $[M]^+$, 330.97 for $[M + Na]^+$. ^1H NMR (DMSO-d_6, 300 MHz): δ (ppm) 11.99 (s, 1H, NH), 10.95 (s, 1H, NH), 8.12 (s, 1H, −CH=), 7.88 (m, 4H, Ph), 7.60 (m, 6H, Ph), 2.25 (s, 3H, CH_3). Anal. Calcd for $C_{17}H_{16}N_4O_2$: C, 66.22; H, 5.23; N, 18.17. Found: C, 65.73; H, 5.07; N, 17.79. IR/cm^{-1} (KBr): ν 3180 (m), 3020 (m), 1653 (vs), 1580 (s), 1533 (s), 1431 (m), 1279 (s), 1138 (s), 1076 (m), 699 (s).

Methylglyoxalbis(N-anilido)osazone ($L^{NHCONHPh}HMe$). To a solution of 4-phenylsemicarbazide (1.51 g, 10 mmol) in methanol (20 mL) was added methylglyoxal (360 mg, 5 mmol), and the resulting mixture was stirred for 15 min at 298 K. A white solid separated out, which was filtered and dried in air. Yield: 1.25 g (73.96%). ESI (positive ion)-MS in CH_3OH: m/z 360.96 for $[M + Na]^+$. ^1H NMR ($CDCl_3$, 300 MHz): δ (ppm) 8.27 (s, 1H, NH), 8.12 (s, 1H, NH), 8.02 (s, 1H, NH), 7.92 (s, 1H, NH), 7.61 (s, =CH−), 7.53 (t, 4H, Ph), 7.34 (m, 4H, Ph,), 7.11 (t, 2H, Ph), 2.17 (s, 3H, CH_3). Anal. Calcd for $C_{17}H_{18}N_6O_2$: C, 60.34; H, 5.36; N, 24.84. Found: C, 59.93; H, 5.24; N, 24.28. IR/cm^{-1} (KBr): ν 3465 (vs), 3229 (s), 1690 (vs), 1586 (s), 1438 (s), 1296 (m), 1149 (s), 918 (s), 762 (s), 661 (s), 614 (s).

*trans-[Os($L^{NHPh}H_2$)(PPh_3)$_2Br_2$] (**3**).* To a hot solution of $L^{NHPh}H_2$ (25 mg, 0.104 mmol) in dry and degassed toluene (30 mL) was added $[Os(PPh_3)_3Br_2]$ (100 mg, 0.0806 mmol), and the resulting mixture was heated at 350 K for 15 min under an argon atmosphere. A green solid separated out, which was filtered and dried in air. Yield: 70 mg (∼63% with respect to osmium). ESI (positive ion)-MS in CH_3OH: m/z 1034.49 for $[\mathbf{3} - Br]^+$. ^1H NMR ($CDCl_3$, 300 MHz): δ (ppm) 8.95 (s, 2H, NH), 7.89 (s, 2H, =CHCH=), 7.69 (m, 12H, Ph, PPh_3), 7.13 (m, 18H, Ph, PPh_3), 6.97 (t, 4H, Ph, NHPh), 6.81 (t, 2H, Ph, NHPh), 5.79 (d, 4H, Ph, NHPh). Anal. Calcd for $C_{52}H_{44}Br_2N_4O_2P_2Os$: C, 53.96; H, 3.99; N, 5.03. Found: C, 53.62; H, 3.89; N, 4.91. IR/cm^{-1} (KBr): ν 3260 (m), 1592 (s), 1482 (s), 1434 (s), 1092 (s), 744 (s), 693 (vs), 517 (vs).

*trans-[Ir($L^{NHPh}H_2$)(PPh_3)$_2Cl_2$] (**4**).* To a hot solution of $L^{NHPh}H_2$ (145 mg, 0.6 mmol) in absolute ethanol (30 mL) were added $IrCl_3$ (0.5 mmol) and PPh_3 (1.2 mmol) successively, and the reaction mixture was refluxed for 60 min (350 K) under an argon atmosphere. A red solid separated out. The solution mixture was cooled to 298 K and filtered. The residue was dried in air and collected. Yield: 220 mg (∼ 43% with respect to iridium). ESI (positive ion)-MS in CH_3CN: m/z 1025.07 for $[M]^+$, 989.02 for $[M - Cl]^+$. Anal. Calcd for $C_{50}H_{44}Cl_2N_4P_2Ir$: C, 58.53; H, 4.32; N, 5.46. Found: C, 57.33; H, 4.24; N, 5.31. IR (KBr): ν 3227 (m), 1600 (m), 1482 (s), 1436 (s), 1188 (m), 1088 (m), 747 (s), 694 (vs), 521 (vs).

*trans-[Ru($L^{NHCOPh}H_2$)(PPh_3)$_2Cl_2$] (**5**).* To a hot solution of $L^{NHCOPh}H_2$ (30 mg, 0.102 mmol) in ethanol (30 mL) was added $[Ru(PPh_3)_3Cl_2]$ (100 mg, 0.104 mmol), and the resulting mixture was heated to reflux for 15 min. A brown solid with some unreacted white $L^{NHCOPh}H_2$ separated out, which was filtered and dried in air. The crude product was further crystallized from a mixture of dichloromethane and *n*-hexane, affording single crystals of **5**. Yield: 40 mg (∼40% with respect to ruthenium). ESI (positive ion)-MS in CH_3OH; m/z 1012.71 for $[M + Na]^+$. ^1H NMR ($CDCl_3$, 300 MHz): δ (ppm) 11.33 (s,1H, NH), 9.51 (s, 1H, NH), 7.65 (m, 12H, Ph, PPh_3), 7.46 (m, 8H, Ph, =CHCH=), 7.33 (d, 4H, Ph), 7.09 (t, 18H, Ph, PPh_3). Anal. Calcd for $C_{52}H_{44}Cl_2N_4O_2P_2Ru$: C, 63.03; H, 4.48; N, 5.65. Found: C, 62.75; H, 4.39 ; N, 5.48. IR/cm^{-1} (KBr): ν 3214 (m), 1654 (vs), 1584 (m), 1542 (vs), 1466 (s), 1435 (s), 1311 (s), 1275 (s), 1144 (s), 1059 (m), 754 (m), 698 (vs), 520 (vs).

*trans-[Os($L^{NHCOPh}H_2$)(PPh_3)$_2Br_2$] (**6**).* To a solution of $L^{NHCOPh}H_2$ (30 mg, 0.102 mmol) in dry and degassed toluene (30 mL) was added $[Os(PPh_3)_3Br_2]$ (100 mg, 0.0806 mmol), and the resulting mixture was heated to reflux for 45 min under an argon atmosphere. A green solid with some unreacted white $L^{NHCOPh}H_2$ separated out, which was filtered and dried in air. Dark green crystals were obtained by slow diffusion of *n*-hexane into the dichloromethane solution of the crude compound. Yield: 50 mg (∼42% with respect to osmium). ESI (positive ion)-MS in CH_3OH: m/z 1167.76 for $[M]^+$. ^1H NMR ($CDCl_3$, 300 MHz): δ (ppm) 11.17 (s, 1H, NH), 9.77 (s, 1H, NH), 7.59 (m, 6H, Ph, PPh_3), 7.54 (m, 14H, Ph, PPh_3), 7.44 (m, 10H, Ph, PPh_3), 7.32 (m, 4H, =CHCH=, Ph), 7.08 (d, 8H, Ph). Anal. Calcd for $C_{52}H_{44}Br_2N_4O_2P_2Os$: C, 53.43; H, 3.79; N, 4.79. Found: C, 53.26; H, 3.73; N, 4.72. IR/cm^{-1} (KBr): ν 3233 (m), 1676 (vs), 1597 (w), 1541 (s), 1482 (m), 1454 (vs), 1272 (vs), 1160 (m), 1088 (m), 747 (m), 698 (vs), 514 (vs).

*trans-[Rh($L^{NHCOPh}H_2$)(PPh_3)$_2Cl_2$] (**7**).* To a hot solution of $L^{NHCOPh}H_2$ ligand (150 mg, 0.5 mmol) in absolute ethanol (30 mL) were added $RhCl_3$ (0.5 mmol) and PPh_3 (1.2 mmol) successively, and the reaction mixture was refluxed for 40 min (350 K) under an argon atmosphere. A red solid separated out. The solution mixture was cooled to 298 K and filtered. The residue was dried in air and collected. Yield: 45 mg (∼ 45% with respect to rhodium). ESI (positive ion)-MS in CH_3CN: m/z 991.35 for $[7]^+$. Anal. Calcd for $C_{52}H_{44}Cl_2N_4O_2P_2Rh$: C, 62.92; H, 4.47; N, 5.64. Found: C, 62.33; H, 4.39; N, 5.51. IR/cm^{-1} (KBr): ν 3465 (m), 1698 (m), 1684 (m), 1586 (w), 1435 (s), 1088 (m), 741 (m), 694 (s), 521 (s).

*trans-[Rh($L^{NHCOPh}HMe$)(PPh_3)$_2Cl$]PF_6 ([**8**]PF_6).* To a hot solution of $L^{NHCOPh}HMe$ ligand (200 mg, 0.6 mmol) in absolute ethanol (30 mL) were added $RhCl_3$ (0.5 mmol) and PPh_3 (1.2 mmol) successively, and the reaction mixture was refluxed for 40 min (350 K) under an argon atmosphere. A clear orange solution was obtained. The solution was cooled to 298 K, and to it was added a solution of sodium hexafluorophosphate in aqueous methanol, and then the mixture was stirred. An orange solid separated out. Orange crystals of [**8**]PF_6·CH_2Cl_2 were obtained by diffusion of *n*-hexane into the dichloromethane solution of the crude product at 298 K. The crystals were used for a single-crystal X-ray diffraction study and other spectral measurements. Yield: 350 mg (63% with respect to rhodium). ESI (positive ion)-MS in CH_3CN: m/z 969.20 for $[\mathbf{8} - Cl]^+$. Anal. Calcd for $C_{53}H_{45}ClF_6N_4O_2P_3Rh$: C, 52.08; H, 4.07; N, 5.02. Found: C, 51.78; H, 4.01; N, 4.94. ^1H NMR ($CDCl_3$, 300 MHz): δ (ppm) 9.21 (s, 1H, NH), 8.78 (s, 1H, −CH=N−), 7.64 (m, 6H, Ph), 7.61 (m, 9H, Ph), 7.42 (m, 12H, Ph), 7.27 (m, 13H, Ph), 2.08 (s, 3H, Me). IR/

dx.doi.org/10.1021/ic4022432 | Inorg. Chem. 2014, 53, 2427−2440

Table 1. Crystallographic Data for 5, 6, [8]PF_6·CH_2Cl_2, and [9]Cl

	5	6	[8]PF_6·CH_2Cl_2	[9]Cl
formula	$C_{52}H_{44}Cl_2N_4O_2P_2Ru$	$C_{52}H_{44}Br_2N_4O_2P_2Os$	$C_{53}H_{45}ClF_6N_4O_2P_3Rh\cdot CH_2Cl_2$	$C_{53}H_{48}Cl_2N_6O_2P_2Ru$
fw	990.82	1168.87	1200.13	1034.88
cryst color	green	green	orange	red
cryst syst	monoclinic	monoclinic	triclinic	orthorhombic
space group	$P2_1/c$	$P2_1/c$	$P\bar{1}$	*Pbca*
a (Å)	19.328(2)	19.182(3)	11.4399(15)	18.0489(12)
b (Å)	15.9729(9)	16.0050(10)	14.218(2)	22.812(2)
c (Å)	17.736(2)	17.914(3)	18.786(4)	24.131(3)
β (deg)	115.605(10)	113.708(12)	100.287(3)	90.00
V (Å^3)	4937.8(8)	5035.6(12)	2625.5(8)	9935.5(16)
Z	4	4	2	8
T (K)	100(2)	100 (2)	100 (2)	100 (2)
calcd density (g cm^{-3})	1.333	1.542	1.518	1.384
no. of rflns collected	162462	114783	81756	198352
no. of unique rflns	25208	14676	18257	18796
no. of rflns $I > 2\sigma(I)$	21990	13611	16071	14250
λ (Å)/μ (mm^{-1})	0.71073/0.533	0.71073/4.225	0.71073/0.637	0.71073/0.534
F(000)	2200	2304	1220	4256
R1[a] ($I > 2\sigma(I)$)/GOF[b]	0.0417/1.104	0.0245/1.131	0.0404/1.071	0.0385/1.070
R1[a] (all data)	0.0252	0.0281	0.0477	0.0623
wR2[c] ($I > 2\sigma$ (I))	0.0643	0.0571	0.1081	0.0818
no. of params/restraints	595/85	563/73	662/0	596/0
residual density (e Å^{-3})	2.681	1.885	3.857	0.636

[a] $R1 = \sum||F_o| - |F_c||/\sum|F_o|$. [b] $GOF = \{\sum[w(F_o^2 - F_c^2)^2]/(n-p)\}^{1/2}$, where $w = 1/[\sigma^2(F_o^2) + (aP)^2 + bP]$ and $P = (F_o^2 + 2F_c^2)/3$. [c] $wR2 = [\sum[w(F_o^2 - F_c^2)^2]/\sum[w(F_o^2)^2]]^{1/2}$.

cm^{-1} (KBr): ν 3344 (m), 1702 (s), 1600 (m), 1480 (s), 1436 (s), 1369 (s), 1340 (s), 1238 (s), 1092 (s), 838 (vs), 744 (s), 696 (vs), 519 (vs).

trans-[Ru(L^{NHCONHPh}HMe)(PPh$_3$)$_2$Cl]Cl ([9]Cl). To a hot solution of L^{NHCONHPh}HMe (35 mg, 0.103 mmol) in ethanol (30 mL) was added [Ru(PPh$_3$)$_3$Cl$_2$] (100 mg, 0.104 mmol), and the resulting mixture was heated to reflux for 20 min. A brown solid separated out, which was filtered and dried in air. The crude product was further crystallized from a solvent mixture of dichloromethane and *n*-hexane. Yield: 65 mg (~63% with respect to ruthenium). ESI (positive ion)-MS in CH_3OH: *m*/*z* 963.65 for [**9** − 2Cl]$^+$. ^{1}H NMR ($CDCl_3$, 300 MHz): δ (ppm) 12.67 (s, 1H, NH), 9.89 (s, 1H, NH), 8.42 (s, 1H, NH), 8.35 (s, 1H, NH), 7.55 (m, 18H, Ph), 7.36 (m, 12H, Ph), 7.06 (m, 11H, Ph, −CH═N−), 2.08 (s, 3H, Me). Anal. Calcd for $C_{53}H_{48}Cl_2N_6O_2P_2Ru$: C, 61.51; H, 4.67; N, 8.12. Found: C, 61.14; H, 4.58; N, 8.02. IR/cm^{-1} (KBr): ν 3271 (m), 1618 (m), 1595 (m), 1499 (s), 1436 (s), 1094 (s), 746 (s), 696 (vs), 519 (vs).

X-ray Crystallographic Data Collection and Refinement of the Structures. Single crystals of **5** (green), **6** (green), [**8**]PF_6·CH_2Cl_2 (orange), and [**9**]Cl (red) were picked up with nylon loops and mounted on a Bruker Kappa-CCD diffractometer equipped with a Mo-target rotating anode X-ray source and a graphite monochromator (Mo Kα, λ = 0.71073 Å). Final cell constants were obtained from least-squares fits of all measured reflections. Structures were readily solved by Patterson methods and subsequent difference Fourier techniques. The crystallographic data are given in Table 1. ShelXS97[7a] and ShelXL97[7b] were used for the structure solution and refinement. All non-hydrogen atoms were refined anisotropically. Hydrogen atoms were placed at calculated positions and refined as riding atoms with isotropic displacement parameters. The phenyl rings comprised of C(16)−C(21) atoms in **5** and C(7)−C(12) atoms in **6** are disordered. Split atom models were refined with restrained thermal displacement parameters, bond distances, and bond angles using the EADP, SADI, and SAME instructions of ShelXL. Occupation ratios were refined to values of about 0.71:0.29 (C(16)−C(21)) and 0.63:0.37 (C(7)−C(12)), respectively, for the disordered phenyl rings of **5** and **6**. Both isomorphous complexes crystallize with one molecule of severely disordered dichloromethane. PLATON SQUEEZE[7c] was used to remove solvent contributions, since modeling of the disorder was not satisfactory.

Though all reported structures can be considered to be of good quality, the following level B alerts were generated by the checkcif procedure. A short distance alert of 1.88 Å was reported for amine proton H(14) and arylic hydrogen H(21) for compounds **5** and **6**, which is due to disorder of the aforementioned phenyl rings; this also explains some elevated thermal displacement parameters. A residual electron density peak of 3.86 e/Å^3 was found at a distance of about 0.84 Å from the Rh ion in [**8**]PF_6·CH_2Cl_2, which is probably due to an imperfect absorption correction and the low temperature of data collection. A small number of 14 low angle reflections out of 18800 independent reflections in the data set of complex [**8**]PF_6·CH_2Cl_2 gave rise to a level B alert. The missing intensities were shielded by the beam stopper due to the large cell volume.

Density Functional Theory (DFT) Calculations. All calculations reported in this article were done with the Gaussian 03W[8] program package supported by GaussView 4.1. The DFT[9] and TD DFT[10] calculations were performed at the level of a Becke three-parameter hybrid functional with the nonlocal correlation functional of Lee−Yang−Parr (B3LYP).[11] Gas-phase geometries of *trans*-[Os(L^{NHPh}H$_2$)(PMe$_3$)$_2$Br$_2$] (**3**^{Me}), *trans*-[Os(L^{NHCOPh}H$_2$)(PMe$_3$)$_2$Br$_2$] (**6**^{Me}), and *trans*-[Ru(L^{NHCONHPh}HMe$^-$)(PMe$_3$)$_2$Cl] ([**9**^{Me}]$^+$), with singlet spin state were optimized using Pulay's direct inversion[12] in the iterative subspace (DIIS), "tight" convergent SCF procedure,[13] ignoring symmetry. Similarly, gas-phase geometries of *trans*-[Os(L^{NHPh}H$_2$)(PMe$_3$)$_2$Cl$_2$] ([**3**^{Me}]$^+$), *trans*-[Ir(L^{NHPh}H$_2$)(PMe$_3$)$_2$Cl$_2$] (**4**^{Me}), *trans*-[Os(L^{NHCOPh}H$_2$)(PMe$_3$)$_2$Cl$_2$] ([**6**^{Me}]$^+$), and *trans*-[Rh(L^{NHCOPh}H$_2$)(PMe$_3$)$_2$Cl$_2$] (**7**^{Me}) were optimized using the doublet spin state. In all calculations, a LANL2DZ basis set along with the corresponding effective core potential (ECP) was used for ruthenium, osmium, rhodium, and iridium metals.[14−16] The valence double-ζ basis set 6-31G[17] for H was used. For the non-hydrogen atoms C, O, P, Cl, and Br valence double-ζ with diffuse and polarization functions, 6-31+G*[18] as basis set was employed for all calculations (the 3-21G[19] basis set was used for C, H, N, O, P, and Cl atoms for **7**^{Me}). Gas-phase geometries of L^{Ph}H$_2$, L^{NHPh}H$_2$, and L^{NHCOPh}H$_2$ were optimized with singlet spin states using the 6-31G[17] basis set. The percentage

dx.doi.org/10.1021/ic4022432 | Inorg. Chem. 2014, 53, 2427−2440

contributions of metal, chloride, bromide, and osazone ligands to the frontier orbitals were calculated using the GaussSum program package.[20] The 60 lowest singlet excitation energies on each of the optimized geometries of $\mathbf{3}^{Me}$, $[\mathbf{3}^{Me}]^+$, $[\mathbf{6}^{Me}]^+$, and $\mathbf{7}^{Me}$ were calculated by the TD DFT method.[21] The natures of transitions were calculated by adding the probability of the same type among α and β molecular orbitals.

RESULTS AND DISCUSSION

Syntheses. All of the complexes of glyoxalbis(*N*-phenyl)osazone ($L^{NHPh}H_2$), glyoxalbis(*N*-benzoyl)osazone ($L^{NHCOPh}H_2$), methylglyoxalbis(*N*-benzoyl)osazone ($L^{NHCOPh}HMe$), and methylglyoxalbis(*N*-anilido)osazone ($L^{NHCONHPh}HMe$) isolated with ruthenium, rhodium, osmium, and iridium ions and their spin states are given in Chart 2. $L^{NHPh}H_2$ is a bidentate NN-donor ligand, while $L^{NHCOPh}H_2$ acts as an NN-donor bidentate as well as NNO-donor tridentate neutral and monoanionic ligands. The binding mode of $L^{NHCONHPh}HMe$ is similar to that of $L^{NHCOPh}HMe$. The binding modes of $L^{NHPh}H_2$, $L^{NHCOPh}H_2$, $L^{NHCOPh}HMe$, and $L^{NHCONHPh}HMe$ in the complexes are shown in Chart 2.

The details of the syntheses of the ligands and their complexes are reported in the Experimental Section. All of the ligands and the complexes have been characterized by elemental analyses and IR, mass, and ^1H NMR spectra; in addition, single-crystal X-ray structure determinations of **5**, **6**, $[\mathbf{8}]PF_6{\cdot}CH_2Cl_2$, and [**9**]Cl have been carried out (vide infra). All of the ligands and the complexes incorporate N−H bonds, stretching frequencies of which are given in Table S1 (Supporting Information). Due to the effects of coordination, the N−H stretching vibrations of the complexes appear comparatively at lower frequencies. UV−vis absorption spectra of $L^{NHPh}H_2$, $L^{NHCOPh}H_2$, $L^{NHCOPh}HMe$, and $L^{NHCONHPh}HMe$ and their complexes were recorded in MeOH at 298 K. The absorption spectra of the ligands are shown in Figure S1 (Supporting Information). The data are summarized in Table 9 (vide infra), and the origin of the absorption of the complexes has been analyzed by TD DFT calculations. All of the ligands absorb strongly in the UV region at around 310 nm due to the $\pi \rightarrow \pi^*$ and $\pi_{nb} \rightarrow \pi^*$ transitions.

Molecular Geometries. Single-crystal X-ray structure determinations have confirmed the trans geometries of **5**, **6**, $[\mathbf{8}]PF_6{\cdot}CH_2Cl_2$, and [**9**]Cl. **5** crystallizes in the $P2_1/c$ space group. The molecular structure in the crystals and the atom-labeling scheme are illustrated in Figure 1. One of the phenyl rings containing C(16)−C(21) atoms of the benzoyl osazone ligand is disordered. The significant bond parameters are summarized in Table 2. In **5**, two PPh_3 ligands are trans to each other. The Ru−N_{imine}, Ru−P, and Ru−Cl distances, 2.0088(7), 2.3823(2), and 2.4509(4) Å, respectively, are consistent with the ruthenium(II) oxidation state and correlate well with those reported for **1**.[5] It is observed that the diimine fragment with the two sp^3-hybridized −NH− functions, two Cl ligands, and the ruthenium(II) ion is planar. The C(2)−N(1) and C(3)−N(4) lengths, 1.3227(11) and 1.3215(10) Å, respectively, are comparatively longer, while the C(2)−C(3) length is comparatively shorter.

6 crystallizes in the $P2_1/c$ space group. The molecular geometry in the crystals and the atom-labeling scheme are shown in Figure 2. Relevant bond parameters are given in Table 3. Two Os−N_{imine} lengths are 2.011(2) and 2.015(2) Å. The Os−P and Os−Br lengths are comparable to those reported in osmium(II) complexes.[22] The bond length trends

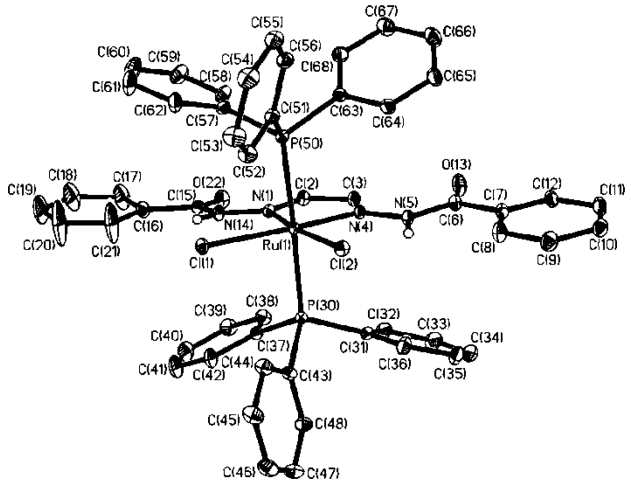

Figure 1. Molecular geometry of **5** in the crystal state (40% thermal ellipsoids; one of the representations of the molecule due to the C(16)−C(21) phenyl ring disorder; H atoms omitted for clarity).

of the imine fragment are significant for analyzing the electronic state of **6**. The average C═N length is 1.328(3) Å, and the C−C length is 1.421(3) Å. The extent of deformation of the diimine fragment is greater in **6** in comparison to that in **5**. Similar to the case for **5**, the diimine ligand with −NHCOPh functions is planar in **6**. One of the phenyl rings with C(7)−C(12) atoms of the diimine ligand is disordered.

$[\mathbf{8}]PF_6{\cdot}CH_2Cl_2$ crystallizes in the $P\bar{1}$ space group. The molecular geometry of $[\mathbf{8}]^+$ ion and the atom-labeling scheme are illustrated in Figure 3. Significant bond parameters are summarized in Table 4. It is to be noted that a residual electron density peak of 3.86 e/Å^3 was found at a distance of about 0.84 Å from the rhodium ion in this crystal structure of $[\mathbf{8}]PF_6{\cdot}CH_2Cl_2$, as stated in the Experimental Section. Although such residual electron density at less than 1 Å to the 4d and 5d transition-metal ions in the X-ray structures is not uncommon,[23] there is a limitation of the metrical parameters of these structures for precise comparison with those of other structures to draw an inference. In the $[\mathbf{8}]^+$ ion, $L^{NHCOPh}HMe$ is a monoanionic tridentate NNO-donor ligand. The $L^{NHCOPh}HMe$ ligand with two five-membered chelate rings and the rhodium(III) ion, excluding the pendant −NHCOPh function, is planar. The RhP_2N_2OCl octahedron is distorted. The two rhodium(III)−N_{imine} distances are notably different. The Rh(1)−N(1) length is 2.038(2) Å, while the Rh(1)−N(4) length is 1.950(2) Å. The Rh−P and Rh−Cl distances are consistent with the rhodium(III) description.[24] The C(2)−N(2) and C(3)−N(4) lengths are 1.314(2) and 1.315(2) Å. The lengths are comparatively longer than that of an imine bond. However, these two imine lengths are shorter than those observed in **5** and **6**. The C(2)−C(3) distance is 1.450(3) Å. The bond parameters of the noncoordinated −HCOPh function are completely different from those of the coordinated $-NCOPh^-$ function. The N(4)−N(5) and N(5)−C(6) lengths are shorter than the N(1)−N(14) and N(14)−C(15) lengths (Table 4). The C(6)−O(13) distance is 1.306(2) Å, while the C(15)−O(22) distance is 1.218 Å. This shows that the negative charge of $L^{NHCOPh}HMe$ is delocalized over the N(5)−C(6)−O(13) fragment.

[**9**]Cl crystallizes in the *Pbca* space group. The molecular geometry of the $[\mathbf{9}]^+$ ion and the atom-labeling scheme are

dx.doi.org/10.1021/ic4022432 | Inorg. Chem. 2014, 53, 2427−2440

Table 2. Selected Experimental Bond Lengths (Å) and Angles (deg) of 5

Ru(1)−N(1)	2.0111(7)	C(2)−C(3)	1.4299(11)
Ru(1)−N(4)	2.0065(7)	N(1)−N(14)	1.3671(10)
Ru(1)−P(30)	2.3775(2)	N(4)−N(5)	1.3687(10)
Ru(1)−P(50)	2.3871(2)	N(5)−C(6)	1.3681(11)
Ru(1)−Cl(1)	2.4535(4)	N(14)−C(15)	1.3687(11)
Ru(1)−Cl(2)	2.4482(3)	O(13)−C(6)	1.2268(11)
N(1)−C(2)	1.3227(11)	O(22)−C(15)	1.2258(11)
N(4)−C(3)	1.3215(10)		
N(1)−Ru(1)−N(4)	77.57(3)	Cl(1)−Ru(1)−Cl(2)	96.487(11)
N(1)−C(2)−C(3)	114.18(7)	Cl(1)−Ru(1)−N(1)	92.86(2)
C(2)−N(1)−Ru(1)	116.88(5)	P(30)−Ru(1)−P(50)	177.149(8)
C(3)−N(4)−Ru(1)	117.00(5)		

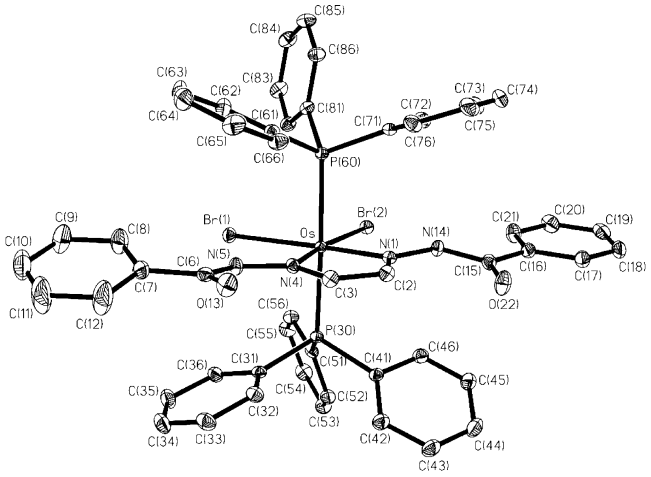

Figure 2. Molecular geometry of **6** in the crystal state (40% thermal ellipsoids; one of the representations of the molecule due to the C(7)−C(12) phenyl ring disorder; H atoms omitted for clarity).

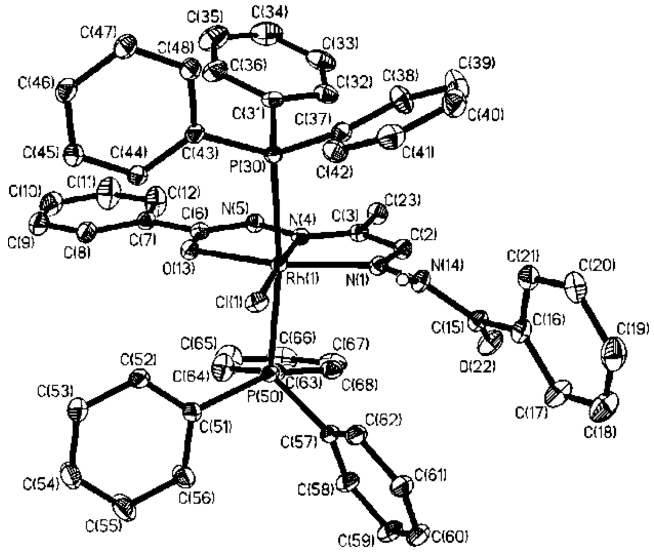

Figure 3. Molecular geometry of $[\mathbf{8}]PF_6 \cdot CH_2Cl_2$ in the crystal state (40% thermal ellipsoids; CH_2Cl_2, $[PF_6]^-$ ion, and H atoms omitted for clarity).

depicted in Figure 4. Relevant bond parameters are summarized in Table 5.

The $L^{NHCONHPh}HMe$ in $[\mathbf{9}]^+$ is a tridentate neutral ligand. The coordinated ligand excluding the pendant −NHCONHPh group is planar. The RuP_2N_2OCl octahedron is distorted. The two Ru−N_{imine} distances are not the same. The Ru(1)−N(4) bond trans to the Ru(1)−Cl(1) bond is shorter than the Ru(1)−N(7) bond. The Ru−P and Ru−Cl lengths are comparable to those observed in **5** and **6**. The two imine bonds C(5)−N(4) = 1.314(2) Å and C(6)−N(7) = 1.328(2) Å are longer, as observed in **1**, **5**, and **6**. The C(5)−C(6) length is 1.431(2) Å. The Cl^- is H-bonded with the coordinated −NHCONHPh function, which displays bond parameters different from those of the noncoordinated −NHCONHPh function. The N(3)−N(4) bond (1.368(2) Å) is shorter than the the N(7)−N(8) bond (1.386(2) Å). Similarly, the N(3)−

Table 3. Selected Experimental Bond Lengths (Å) and Angles (deg) of 6 and Corresponding Calculated Parameters of 6^{Me}

	exptl (**6**)	calcd (6^{Me})		exptl (**6**)	calcd (6^{Me})
			Bond Lengths		
Os−N(1)	2.0112(19)	2.0358	C(2)−C(3)	1.421(3)	1.415
Os−N(4)	2.0146(18)	2.0342	N(1)−N(14)	1.374(2)	1.375
Os−P(30)	2.3900(5)	2.4120	N(4)−N(5)	1.378(2)	1.376
Os−P(60)	2.3825(5)	2.4097	N(5)−C(6)	1.373(3)	1.379
Os−Br(1)	2.5838(5)	2.6700	N(14)−C(15)	1.368(3)	1.379
Os−Br(2)	2.5846(4)	2.668	O(13)−C(6)	1.224(3)	1.231
N(1)−C(2)	1.329(3)	1.332	O(22)−C(15)	1.227(3)	1.231
N(4)−C(3)	1.328(3)	1.333			
			Bond Angles		
N(1)−Os−N(4)	76.80(7)	77.01	Br(1)−Os−Br(2)	94.987(15)	95.71
N(1)−C(2)−C(3)	114.15(19)	114.82	Br(1)−Os−N(4)	93.74(5)	93.67
C(2)−N(1)−Os	117.50(15)	116.66	P(30)−Os−P(60)	176.518(19)	169.09
C(3)−N(4)−Os	117.62(14)	116.70			

dx.doi.org/10.1021/ic4022432 | Inorg. Chem. 2014, 53, 2427−2440

Table 4. Selected Experimental Bond Lengths (Å) and Angles (deg) of [8]PF_6·CH_2Cl_2

Rh(1)−N(1)	2.0378(16)	C(2)−C(3)	1.450(3)
Rh(1)−N(4)	1.9498(15)	C(3)−C(23)	1.492(2)
Rh(1)−P(30)	2.3836(6)	N(1)−N(14)	1.374(2)
Rh(1)−P(50)	2.4040(6)	N(4)−N(5)	1.359(2)
Rh(1)−Cl(1)	2.3804(5)	N(5)−C(6)	1.332(2)
Rh(1)−O(13)	2.0815(14)	N(14)−C(15)	1.400(2)
N(1)−C(2)	1.314(2)	O(13)−C(6)	1.306(2)
N(4)−C(3)	1.315(2)	O(22)−C(15)	1.218(2)
N(1)−Rh(1)−N(4)	79.32(6)	P(30)−Rh(1)−P(50)	171.113(17)
O(13)−Rh(1)−Cl(1)	105.30(4)	N(1)−C(2)−C(3)	116.64(17)
O(13)−Rh(1)−N(4)	77.85(6)	C(2)−N(1)−Rh(1)	113.04(12)
Cl(1)−Rh(1)−N(1)	97.53(4)	C(3)−N(4)−Rh(1)	118.35(12)

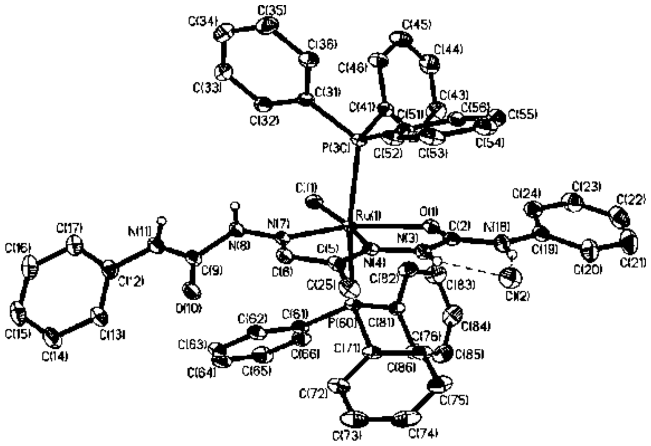

Figure 4. Molecular geometry of [**9**]Cl in the crystal state (40% thermal ellipsoids; H atoms omitted for clarity).

C(2) bond is shorter than the N(8)−C(9) bond. The C(2)−O(1) length is 1.261(2) Å, while the C(9)−O(10) length is 1.215(2) Å.

EPR Spectra. Magnetic susceptibility measurements at 298 K confirmed the paramagnetism of **4** and **7** (μ_{eff} = 1.82 and 1.76 μ_B). The EPR spectra of **4** and **7** were recorded in the solid state at 298 K and as frozen glasses at 130 K. The spectra are shown in Figure 5. The parameters of the EPR measurements are given in Table S4 (Supporting Information), and the simulated g values and the coupling constants are summarized in Table 6. The g_{av} values are consistent with the existence of osazone anion radicals in the solids of **4** and **7**. The g_{av} values are 1.989 and 2.028, respectively, in **4** and **7**. However, in solution the contributions of iridium(II) and rhodium(II) ions in **4** and **7** are significantly greater. The anisotropicities (Δg) of the g values of the frozen glasses of **4** and **7** are respectively 0.189 and 0.238. The hyperfine couplings due to ^{193}Ir and ^{103}Rh are also noted (Table 6).[25] We have remeasured the EPR spectrum of the frozen CH_2Cl_2 glass of **2**, and the spectrum is shown in Figure 5h. The g values without simulation were misreported in a previous article.[6] In frozen glass, similar to the case for **4** and **7**, a significant metal contribution to **2** was authenticated (g_{av} = 2.055, Table 6).

The EPR spectra of the electrogenerated $\mathbf{3}^+$, $\mathbf{5}^+$, and $\mathbf{6}^+$ ions were recorded in CH_2Cl_2 frozen glasses at 130 K. The spectra are illustrated in Figure 5e−g, and the EPR parameters are summarized in Table 6. The g parameters of the $\mathbf{3}^+$ ion (g_1 = 2.461, g_2 = 2.103, g_3 = 1.841) are consistent with the formation of the osmium(III) complex *trans*-$[Os^{III}(L^{NHPh}H_2)(PPh_3)_2Br_2]^+$. The result correlates well with the g parameters of *trans*-$[Ru^{III}(L^{NHPh}H_2)(PPh_3)_2Cl_2]^+$ upon oxidation of **1**.[5] The EPR spectra of $\mathbf{5}^+$ and $\mathbf{6}^+$ ions are similar to that of the $\mathbf{3}^+$ ion and are rhombic in nature, corresponding to the existence of ruthenium(III) and osmium(III) ions in these cations. This authenticates that the oxidation of **5** and **6** affords ruthenium(III) and osmium(III) complexes of benzoyl osazone as *trans*-

Table 5. Selected Experimental Bond Lengths (Å) and Angles (deg) of [9]Cl and Corresponding Calculated Parameters of $[\mathbf{9}^{Me}]^+$

	exptl [9]Cl	calcd $[\mathbf{9}^{Me}]^+$		exptl [9]Cl	calcd $[\mathbf{9}^{Me}]^+$
		Bond Lengths			
Ru(1)−N(4)	1.9467(14)	1.9794	N(3)−N(4)	1.3680(19)	1.3817
Ru(1)−N(7)	2.0324(14)	2.0327	N(7)−N(8)	1.386(2)	1.3539
Ru(1)−P(30)	2.3855(5)	2.4297	N(3)−C(2)	1.365(2)	1.4016
Ru(1)−P(60)	2.3872(4)	2.4257	N(8)−C(9)	1.415(2)	1.4105
Ru(1)−Cl(1)	2.4289(5)	2.5082	C(2)−N(18)	1.341(2)	1.3534
Ru(1)−O(1)	2.2326(12)	2.2970	C(9)−N(11)	1.358(2)	1.3676
N(4)−C(5)	1.314(2)	1.3212	O(1)−C(2)	1.261(2)	1.2484
N(7)−C(6)	1.328(2)	1.3274	O(10)−C(9)	1.215(2)	1.2256
C(5)−C(6)	1.431(2)	1.4404			
		Bond Angles			
N(4)−Ru(1)−N(7)	78.14(6)	78.42	O(1)−Ru(1)−Cl(1)	111.29(3)	111.68
N(4)−C(5)−C(6)	111.73(15)	112.87	O(1)−Ru(1)−N(4)	76.42(5)	75.62
C(5)−N(4)−Ru(1)	119.93(12)	118.29	P(30)−Ru(1)−P(60)	165.393(16)	165.69
C(6)−N(7)−Ru(1)	113.66(11)	114.38			

dx.doi.org/10.1021/ic4022432 | Inorg. Chem. 2014, 53, 2427−2440

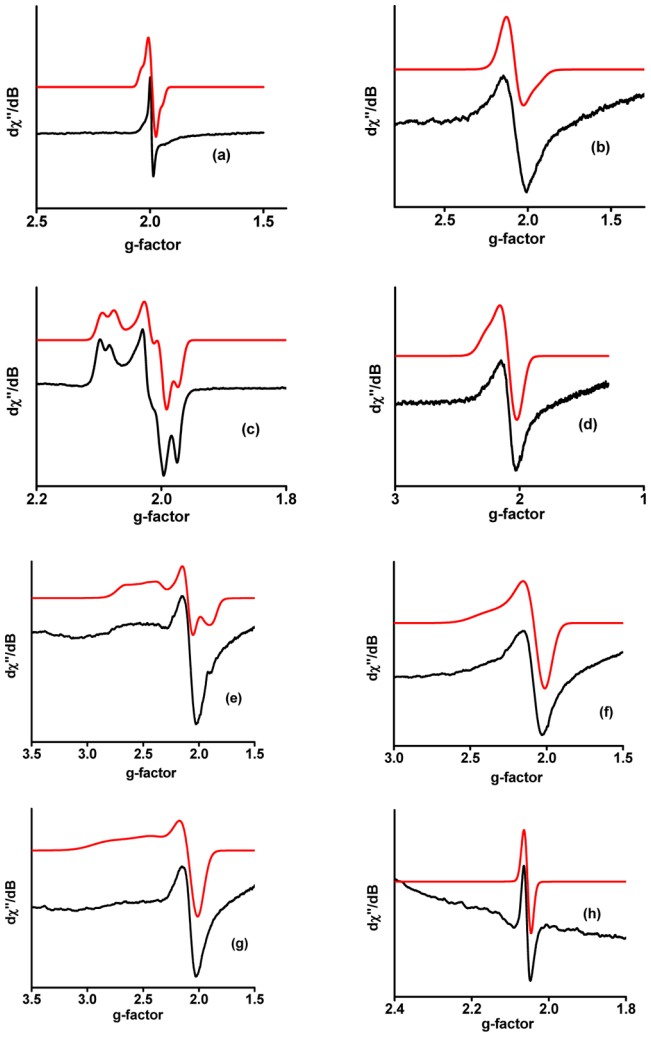

Figure 5. X-band EPR spectra of (a) **4** (solid) at 298 K, (b) **4** (CH_2Cl_2 frozen glass) at 130 K, (c) **7** (solid) at 298 K, (d) **7** (CH_2Cl_2 frozen glass) at 130 K, (e) $\mathbf{3}^+$ (CH_2Cl_2 frozen glass) at 130 K, (f) $\mathbf{5}^+$ (CH_2Cl_2 frozen glass) at 130 K, (g) $\mathbf{6}^+$ (CH_2Cl_2 frozen glass) at 130 K, and (h) **2** (CH_2Cl_2 frozen glass) at 77 K. Black lines denote experimental spectra and red lines simulated spectra.

$[Ru^{III}(L^{NHCOPh}H_2)(PPh_3)_2Cl_2]^+$ ($\mathbf{5}^+$) and *trans*-$[Os^{III}(L^{NHCOPh}H_2)(PPh_3)_2Br_2]^+$ ($\mathbf{6}^+$).

Electrochemical Studies. The redox activities of the complexes in CH_2Cl_2 were investigated by cyclic voltammetry at 298 K. The cyclic voltammograms are shown in Figure 6, and the redox potential data referenced to the ferrocenium/ferrocene (Fc^+/Fc) couple are summarized in Table 7. The anodic wave of **3** (Figure 6b) at −0.04 V ($E_{1/2}$[2]) is reversible and is assigned to a Os^{III}/Os^{II} couple. In the ruthenium analogue **1**, a similar Ru^{III}/Ru^{II} couple appears at 0.40 V.[5] It corresponds to the greater extent of mixing of the metal d orbitals with the π^* orbital in **3**. The result is consistent with the diffuseness of the 5d orbital of osmium. The two-electron quasi-reversible anodic peak (E_P[3]) at 0.80 V is due to the oxidation of the $L^{NHPh}H_2$ ligand, as shown in Scheme 2. The deprotonation of the $L^{NHPh}H_2$ ligand was confirmed by the IR spectrum of the crude electrochemically oxidized product, as illustrated in Figure S4 (Supporting Information). A similar but completely irreversible redox peak has also been observed in **1** and the free $L^{NHPh}H_2$ ligand, respectively, at 0.70 and 0.30 V at 298 K.

Both the anodic and cathodic redox waves of **4** and **7** are irreversible. The anodic peak potentials of **2**, **4**, and **7** (**2**, +0.13 V; **4**, +0.48 V; **7**, +0.70 V) depend on the metal ions, showing the significant contributions of the metal ions to the SOMOs of these paramagnetic molecules in solution. The essence is that, when the unpaired electron is localized on the ligand, the anodic peak potentials of the complexes are expected to be comparable, while if the unpaired electron is localized on the metal ion, the anodic peak potential will be metal ion dependent. The EPR spectra of these two states are different. The metal-dependent peak potentials are consistent with the EPR spectra (Table 6), which reveal that in solids of **2**, **4**, and **7** the unpaired electron is localized on the ligand but in solution the unpaired electron is also delocalized over the metal ions. The rhodium(III)/rhodium(II) reduction potentials of **2** and **7** are comparable. The oxidation and reduction potentials are separated by −1.99 V in **7**. However, the anodic and cathodic peaks of **2** appear respectively at +0.13 and −1.22 V (separated by 1.35 V). One of the significant results is that the $\mathbf{2}^+$ ion (Chart 1) was successfully isolated and characterized by a single-crystal structure determination.[6] The electronic states of the products after reductions of $\mathbf{2}^+$, $\mathbf{4}^+$, and $\mathbf{7}^+$ ions have been analyzed by EPR spectra. The EPR spectra of the reduced species of the oxidized analogues were recorded in CH_2Cl_2–toluene frozen glass at 130 K. The spectra are similar to the corresponding EPR spectra of **2**, **4**, and **7** in frozen glasses with the same anisotropic g values. The EPR parameters (solids, solutions, and frozen glasses) and the redox potential data of **2**, **4**, and **7** are consistent with a significant contribution of the nonradical tautomer **B** to the $[M^{III}(L^{NHAr}H_2^{\bullet-})(PPh_3)_2Cl_2$ (**A**) ↔ $[M^{II}(L^{NHAr}H_2)(PPh_3)_2Cl_2$ (**B**)] equilibria in solution in comparison to the case in solids, in which tautomer **A** incorporating osazone anion radical dominates.

Electronic Structures. The electronic structures of the osazone complexes to correlate the redox couples at

Table 6. X-Band EPR Spectral Parameters of 2, 4, 7, [3]PF_6, [5]PF_6, and [6]PF_6[a]

complex	conditions	g_1	g_2	g_3	g_{iso}/g_{av}	Δg	line width/mT
2	CH_2Cl_2 frozen glass (77 K)		2.055		2.055		2.5
4	solid (295 K)		1.9895		1.9895	0	4.5 ("^{193}Ir"; A_1 = 0 G, A_2 = 52 G, A_3 = 0 G)
	CH_2Cl_2 frozen glass (130 K)	2.1230	2.0992	1.9339	2.0520	0.189	12.5 ("^{193}Ir"; A_1 = 32 G, A_2 = 0, A_3 = 61G)
7	solid (295 K)	2.0880	2.0106	1.9847	2.0277	0.103	2.5 ("^{103}Rh"; A_1 = 32 G, A_2 = 32 G, A_3 = 36 G)
	CH_2Cl_2 frozen glass (130 K)	2.227	2.091	1.989	2.102	0.238	13.5 ("^{103}Rh"; A_1 = 143 G, A_2 = 0 G, A_3 = 57 G)
[3]PF_6	CH_2Cl_2 frozen glass (130 K)	2.4611	2.1029	1.8405	2.1348	0.621	8.0 ("^{189}Os"; A_1 = 118 G, A_2 = 0 G, A_3 = 68 G)
[5]PF_6	CH_2Cl_2 frozen glass (130 K)	2.2425	2.0819	2.0508	2.1250	0.192	16.0 ("^{101}Ru"; A_1 = 107 G, A_2 = 18 G, A_3 = 0 G)
[6]PF_6	CH_2Cl_2 frozen glass (130 K)	2.551	2.091	1.999	2.213	0.552	18.0 ("^{189}Os"; A_1 = 168 G, A_2 = 21 G, A_3 = 0 G)

[a] $\Delta g = g_{max} - g_{min}$. line width = peak-to-peak width of the spectrum.

dx.doi.org/10.1021/ic4022432 | Inorg. Chem. 2014, 53, 2427−2440

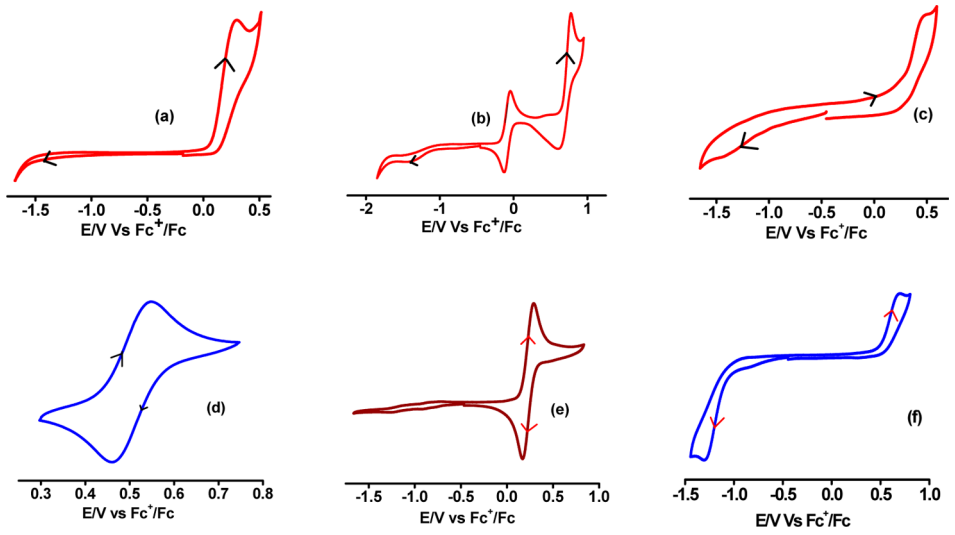

Figure 6. Cyclic voltammograms of (a) $L^{NHPh}H_2$ (sr (scan rate, in mV/s) 100), (b) **3** (sr: 100), (c) **4** (sr: 100), (d) **5** (sr: 100), (e) **6** (sr: 100), and (f) **7** (sr: 50 mV/s) in CH_2Cl_2 at 298 K. Conditions: 0.20 M $[N(n\text{-}Bu)_4]PF_6$ supporting electrolyte; platinum working electrode.

Table 7. Redox Potentials of $L^{NHPh}H_2$ and Complexes 1−7 in CH_2Cl_2[a]

	E_p^1/V	$E_{1/2}^2$/V (ΔE/mV)	E_p^3/V
$L^{NHPh}H_2$			+0.30
1		+0.391	+0.7
2	−1.22		+0.13
3		−0.04 (79)	+0.81
4	−1.43		+0.48
5		+0.505 (90)	
6		+0.237 (119)	
7	−1.29		+0.698

[a]Conditions: 0.20 M $[N(n\text{-}Bu)_4]PF_6$) at 298 K (referenced to ferrocenium/ferrocene, Fc^+/Fc, couple). E_p^1 = cathodic peak potential; ΔE = peak-to-peak separation; E_p^3 = anodic peak potential.

Scheme 2

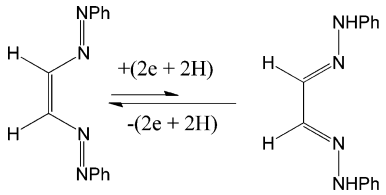

comparatively lower potentials and lower energy absorption bands of **3**, **5**, and **6** and the ligand-centered EPR spectra of **4** and **7** in solids were elucidated by the density functional theory (DFT) calculations. The gas phase geometries of $L^{Ph}H_2$, $L^{NHPh}H_2$, $L^{NHCOPh}H_2$, *trans*-$[Os(L^{NHPh}H_2)(PMe_3)_2Br_2]$ ($\mathbf{3}^{Me}$), *trans*-$[Os(L^{NHCOPh}H_2)(PMe_3)_2Br_2]$ ($\mathbf{6}^{Me}$) and *trans*-$[Ru(L^{NHCONHPh}HMe^-)(PMe_3)_2Cl]^+$ $[\mathbf{9}Me]^+$ with singlet spin states and *trans*-$[Os(L^{NHPh}H_2)(PMe_3)_2Cl_2]^+$ $[\mathbf{3}^{Me}]^+$, *trans*-$[Ir(L^{NHPh}H_2)(PMe_3)_2Cl_2]$ ($\mathbf{4}^{Me}$), *trans*-$[Os(L^{NHCOPh}H_2)(PMe_3)_2Cl_2]^+$ $[\mathbf{6}^{Me}]^+$, and *trans*-$[Rh(L^{NHCOPh}H_2)(PMe_3)_2Cl_2]$ ($\mathbf{7}^{Me}$) with doublet spin states were optimized. All of the optimized geometries are shown in Figure S3 (Supporting Information).

The calculated bond parameters of $\mathbf{6}^{Me}$ are given in Table 3, and those of $[\mathbf{9}^{Me}]^+$ are given in Table 5. The significant optimized bond lengths of $\mathbf{3}^{Me}$, $\mathbf{4}^{Me}$, and $\mathbf{7}^{Me}$ are summarized in Table 8. The ground electronic state of **3** can be defined by the

Table 8. Selected Calculated Bond Lengths (Å) of $\mathbf{3}^{Me}$, $\mathbf{4}^{Me}$, and $\mathbf{7}^{Me}$

	3	**4**	**7**
M-P	2.672 2.669	2.470 2.469	2.506 2.495
M-X	2.405 2.416	2.400 2.403	2.408 2.407
M-N2	2.034	2.063	2.040
M-N5	2.032	2.061	2.042
N1-N2	1.371	1.394	1.406
N2-C3	1.335	1.353	1.362
C3-C4	1.410	1.392	1.394
N5-C4	1.335	1.352	1.363
N5-C6	1.371	1.394	1.409

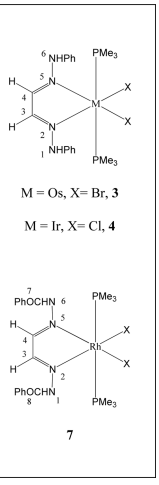

resonance structures of closed-shell singlet ($\mathbf{3}^{Os(II)}$) and diradical open-shell singlet ($\mathbf{3}^{Os(III)L\bullet-}$) states, as illustrated in Chart 3.

Chart 3

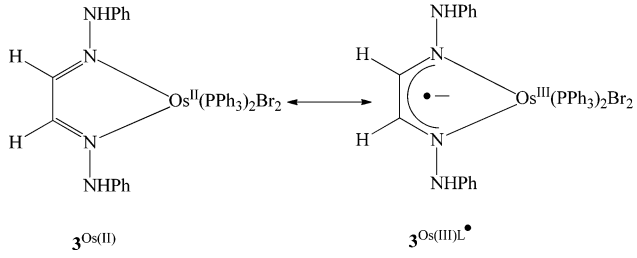

The bond parameters of these two states are significantly different. The calculated C═N lengths (1.335 Å, Table 8) are longer, while the C−C length (1.410 Å) of the diimine fragment is comparatively shorter. The trend corresponds to that of a diimine anion radical.[2,6] However, the closed-shell singlet solution of $\mathbf{3}^{Me}$ is stable. No instability due to open-shell

dx.doi.org/10.1021/ic4022432 | Inorg. Chem. 2014, 53, 2427−2440

singlet (OSS) perturbation has been observed. The possibility of a diradical ground electronic state ($3^{Os(III)L\bullet}$) of **3** has been omitted. Molecular orbital analyses have established an effective mixing of the π^* orbital with the osmium d orbitals. This results in a delocalization of the metal electron to the diimine fragment. Bond lengths of the diimine fragment qualitatively show that the electron transfer occurs to the extent of 0.6e to the π^* orbital. The features are similar to those observed in the case of **1**, where ruthenium to osazone ligand electron transfer occurs to the extent of 0.3e.[5] The paramagnetic 3^+ cation is an osmium(III) complex. The Mulliken spin density distribution of the $[3^{Me}]^+$ ion is illustrated in Figure 7c.

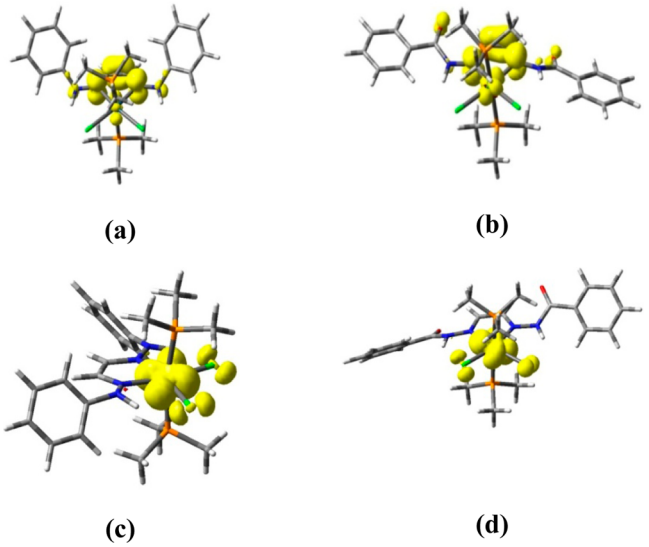

Figure 7. Spin density plots of (a) 4^{Me} (isovalue 0.004), (b) 7^{Me} (isovalue 0.004), (c) $[3^{Me}]^+$ (isovalue 0.004), and (d) $[6^{Me}]^+$ (isovalue 0.004) values from Mulliken spin population analyses. Spin density for 4^{Me}: N1, 0.01; N2, 0.31; C3, 0.13; C4, 0.12; N5, 0.32; N6, 0.01; Ir, 0.02. Spin density for 7^{Me}: N2, 0.29; C3, 0.07; C4, 0.12; N5, 0.26; O7, 0.03; O8, 0.05; Rh, 0.11. Spin density for $[3^{Me}]^+$: Os, 0.86; Cl(1), 0.087; Cl(2), 0.08. Spin density for $[6^{Me}]^+$: Os, 0.92; Cl(1), 0.12; Cl(2), 0.12. The numbering scheme is shown in the illustration of Table 8.

In contrast, the calculated bond parameters of the $L^{NHPh}H_2$ ligand of 4^{Me} correlate well with those of the reduced $L^{NHPh}H_2^{\bullet-}$ ligand, as observed in **2**, which incorporates a phenyl osazone anion radical. Mulliken spin population analyses establish that the spin density is mainly localized on the diimine fragment, as depicted in Figure 7a. The features correlate well with the existence of $L^{NHPh}H_2^{\bullet-}$, which was confirmed by the solid-state EPR spectrum of **4** at 298 K. Thus, the ground electronic state of **4** is defined by the resonance structure $4^{L\bullet}$, as illustrated in Chart 4. In the solid state, the contribution of $4^{Ir\bullet}$ to the ground electronic state has not been justified. However, the contribution of $4^{Ir\bullet}$ in solution has been authenticated by an EPR spectrum.

The calculated bond parameters for $L^{NHCOPh}H_2$ of 6^{Me} (Table 3) are comparable to those of 3^{Me}. The calculated average C═N and C−C lengths of the diimine fragment of $L^{NHCOPh}H_2$ are 1.332 and 1.415 Å, respectively. The single-crystal X-ray structure determinations have confirmed that −CH═N bond lengths (**5**, 1.321(2) Å; **6**, 1.328(1) Å) of the $L^{NHCOPh}H_2$ ligand in **5** and **6** are longer while the C−C length (**5**, 1.431(2) Å; **6**, 1.421(3) Å) is shorter (Tables 2 and 3) than

Chart 4

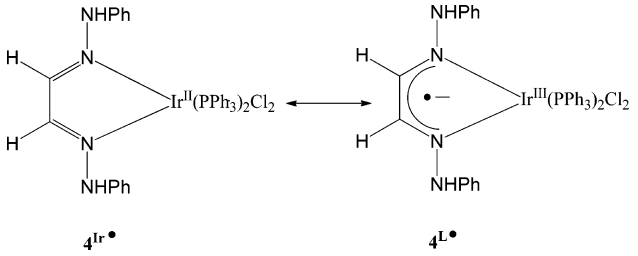

those observed in a free diimine ligand (C═N, 1.24 Å; C−C, 1.44 Å).[1] To explain these features, the resonance structures of **5** and **6** have been considered, as shown in Chart 5.

Chart 5

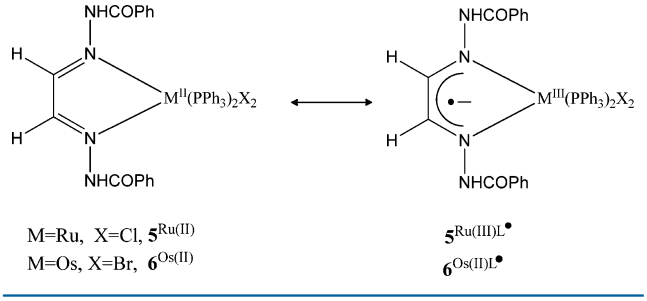

Similar to the case for **1** and **3**, the closed-shell singlet (CSS) solution of 6^{Me} is stable. No perturbation due to an open-shell singlet (OSS) has been noted. The ground electronic states of **5** and **6** thus cannot be defined by the diradical $5^{Ru(III)L\bullet}$ and $6^{Os(III)L\bullet}$ states as illustrated in Chart 5,; rather, they are defined by the $5^{Ru(II)}$ and $6^{Os(II)}$ states (Chart 5). The calculated bond parameters of 6^{Me} correlate well with those observed experimentally (Tables 2 and 3). The comparatively longer C═N lengths of the $L^{NHCOPh}H_2$ ligand of **5** and **6** have been analyzed by the mixing of the metal d with the π^* orbitals, resulting in the delocalization of the metal electron to the π^* orbital. Due to the relativistic expansion of the d orbitals of osmium(II) ion, the extent of electron transfer in **6** is greater than that in **5**. A similar trend has been established in the case of **3** in comparison to **1**. The effect has been noted in the redox potential data also. The anodic redox couples of **3** and **6** are more negative, in comparison to those of **1** and **5**. Similar to the case for the 3^+ ion, 6^+ is a osmium(III) complex, and this has been authenticated by the Mulliken spin density distribution of $[6^{Me}]^+$ ion as depicted in Figure 7d.

The calculated bond parameters of **7** are comparable to those of **2** and **4**. The C═N and C−C bond lengths are consistent with those of the $L^{NHPh}H_2^{\bullet-}$ present in **2** and **4**. Mulliken spin population analysis affirms that the spin is mainly localized on the $L^{NHCOPh}H_2$ ligand, as shown in Figure 7b. The features correlate well with the ligand-centered EPR spectrum of solids of **7** (Figure 5b). Thus, the ground electronic state of **7** is defined by the $7^{L\bullet}$ state, as depicted in Chart 6. In the solid state, no major contribution of the $7^{Rh\bullet}$ state has been recorded in the EPR spectra or in the spin density plot (Figure 7b). However, the existence of the $7^{Rh\bullet}$ state in solution has been detected by an EPR spectrum.

The calculated bond parameters of $L^{NHCONHPh}HMe$ in $[9^{Me}]^+$ (Table 5) and the X-ray parameters of $[8]PF_6{\cdot}CH_2Cl_2$ and [**9**]Cl are comparable to those of **1**, **5**, and **6**, corresponding to the

dx.doi.org/10.1021/ic4022432 | Inorg. Chem. 2014, 53, 2427−2440

Chart 6

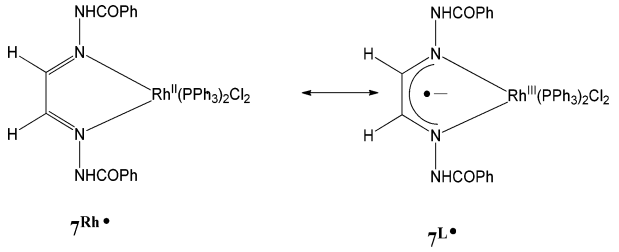

closed-shell singlet ground state. $\mathbf{8}^+$ and $\mathbf{9}^+$ cations thus have been defined as rhodium(III) and ruthenium(II) complexes of monoanionic $L^{NHCOPh}HMe$ and neutral $L^{NHCONHPh}HMe$ ligands, respectively.

Electronic Spectra. UV/vis/near-IR absorption spectra of the complexes were recorded in CH_2Cl_2 solvent at 298 K. The spectral data are given in Table 9. Selected spectra are shown in Figure 8. It was reported that a strong mixing of the ruthenium d orbitals with the π^* orbital occurs in complex **1**.[5] Due to this metal to ligand charge transfer (MLCT), **1** displays a lower energy absorption band. Free $L^{NHPh}H_2$ ligand absorbs at 310 nm, while **1** absorbs at 406 and 534 nm. **3**, with a 5d metal osmium ion, displays a broad absorption band spanning at 800−300 nm with maxima at 671, 552, and 414 nm. Similar to the case for **2**, $L^{NHPh}H_2$ is reduced in **4**, which absorbs weakly at 546 nm.

Table 9. UV/Vis/Near-IR Absorption Spectral Data of the Ligands and Complexes at 298 K

substrate	solvent	λ_{max}/nm (ε/10^4 M^{-1} cm^{-1})
$L^{NHCOPh}H_2$	MeOH	372 (2.81), 300 (0.55)
$L^{NHCOPh}H_2$	MeOH	355 (1.16), 336 (2.36), 323 (2.58), 250 (2.89)
$L^{NHCOPh}HMe$	MeOH	312 (2.01)
$L^{NHCONHPh}HMe$	MeOH	303 (1.43)
1	CH_2Cl_2	534 (0.23), 406 (2.06), 318 (0.57), 272 (3.06), 237 (3.27)
2	CH_2Cl_2	443 (3.1), 352 (9.3)
3	CH_2Cl_2	671 (0.05), 550 (0.17), 414 (2.09), 308 (0.68)
$\mathbf{3}^+$	CH_2Cl_2	666 (0.16), 482 (0.84), 412 (1.27), 328 (1.14)
4	CH_2Cl_2	546 (0.08), 445 (0.12), 366 (0.19)
5	CH_2Cl_2	552 (0.09), 453 (0.27), 346 (0.86), 279 (1.61)
6	CH_2Cl_2	907 (0.04), 623 (0.08), 446 (0.43), 344 (1.32), 258 (2.35)
$\mathbf{6}^+$	CH_2Cl_2	740 (0.06), 523 (0.26), 441 (0.66), 352 (2.21)
7	CH_2Cl_2	468 (0.56), 372 (1.26), 329 (2.09), 272 (1.65)
[**8**]PF_6	CH_2Cl_2	519 (0.28), 488 (0.3), 339 (1.61)
[**9**]Cl	CH_2Cl_2	553 (0.02), 422 (0.15), 351 (0.09), 276 (1.57)

Similar absorption features were observed with $L^{NHCOPh}H_2$ ligand and its complexes. The free $L^{NHCOPh}H_2$ ligand absorbs at 314 nm, while its complex **5** absorbs at 552 and 453 nm. The osmium analogue **6** absorbs at much lower energy with bands at 907, 623, and 446 nm. In **7**, $L^{NHCOPh}H_2$ is reduced and the comparatively lower energy absorption bands disappear, as observed in the cases of complexes **2** and **4**. [**8**]PF_6 absorbs at 519 nm, while [**9**]Cl with a neutral ligand displays absorption bands at 553 and 422 nm. The spectrum of [**9**]Cl is shown in Figure S2 (Supporting Information).

The origin of the lower energy absorption bands of the complexes was elucidated by time-dependent (TD) DFT calculations on $\mathbf{3}^{Me}$ and $\mathbf{7}^{Me}$. The excitation energies with the oscillator strengths and the transition types are summarized in Table S2 (Supporting Information). Analyses of the singlet transition of $\mathbf{3}^{Me}$ authenticated that the lower energy absorption bands of **3**, **5**, and **6** at >400 nm are due to metal to ligand charge transfer (MLCT). The calculated excitation energies of the MLCT transitions of $\mathbf{3}^{Me}$ are 681.62, 421.30, and 407.14 nm, which correlate well with the experimental absorption bands of **3** at 641, 548, and 414 nm in CH_2Cl_2 solvent. The conversion $\mathbf{3} \rightarrow \mathbf{3}^+$ undergoes several isosbestic points, which are determined by spectroelectrochemical measurements and are shown in Figure 9a. During the conversion, the intensity of the strong MLCT band of **3** at 414 nm gradually decreases, generating new absorption features at 330 and 490 nm.

Similar spectral features during the conversion $\mathbf{6} \rightarrow \mathbf{6}^+$ have been determined by spectroelectrochemical measurements and are shown in Figure 9b. Origins of transitions in $\mathbf{3}^+$ and $\mathbf{6}^+$ were elucidated by TD DFT calculations on $[\mathbf{3}^{Me}]^+$ and $[\mathbf{6}^{Me}]^+$ ions (Table S2, Supporting Information). It is noted that both cations absorb at lower energy due to the d−d and MLCT transitions. The absorption band of $\mathbf{3}^+$ ion at 666 nm is assigned to the d−d transition, while that at 482 nm is assigned to the d−d and MLCT transitions. Similar features are observed in the case of $\mathbf{6}^+$ ion also.

The absorption spectral features of **4** and **7** are similar. The TD DFT calculations on $\mathbf{7}^{Me}$ established that the lower energy absorptions of these anion radical complexes are due to the $\pi \rightarrow \pi^*$ transition. The calculated $\pi \rightarrow \pi^*$ excitation energies of $\mathbf{7}^{Me}$ at 540.05, 520.97, and 492.88 nm (Table S2, Supporting Information) are consistent with the broad absorption band of **7** in CH_2Cl_2 peaking from 540 nm with a λ_{max} value at 468 nm. The $\pi_{SOMO} \rightarrow \pi_{aromatic}^*$ (α), $\pi \rightarrow \pi^*$ (β), and $\pi \rightarrow d_{Rh}$ (α) transitions are the origins of these lower energy absorption bands.

The solid-state absorption spectra (Kubelka−Munk plots)[26] of **2**, **4**, and **7** were determined by the diffuse reflection method. The spectra are shown in Figure 10. It is significant to observe that the solid-state absorption spectra of these complexes are metal independent. The absorptions are due to $\pi \rightarrow \pi^*$ transitions, while the solution spectra are significantly different (Figure 8) due to the contribution of the metal ions to the ground electronic state.

CONCLUSION

In two previous articles we reported the coordination chemistry of phenyl osazone with ruthenium(II/III) and rhodium(III) ions, and these works established that phenyl osazone is redox noninnocent. In this article, in conjunction with the osmium and iridium complexes of phenyl osazone, we have established the coordination chemistry of benzoyl osazone and anilido osazone with ruthenium, osmium, and rhodium. The work reports the hitherto unknown benzoyl osazone anion radical complex of the rhodium(III) ion. Moreover, the different binding modes of the benzoyl and anilido osazones have been analyzed. Further, this work authenticates the different ground electronic structures of the osazone complexes of rhodium and iridium ions in the solid state and solution. In addition to phenyl osazone ($L^{NHPh}H_2$), the coordination chemistry of benzoyl osazones ($L^{NHCOPh}HR$; R = H, Me) and anilido

dx.doi.org/10.1021/ic4022432 | Inorg. Chem. 2014, 53, 2427−2440

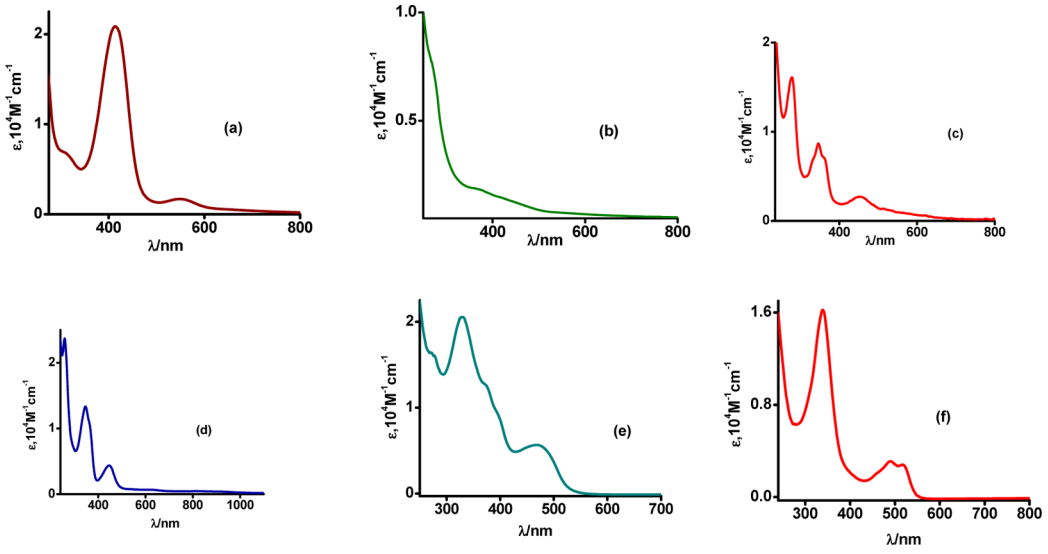

Figure 8. UV/vis/near-IR spectra of (a) **3**, (b) **4**, (c) **5**, (d) **6**, (e) **7**, and (f) [**8**]PF_6.

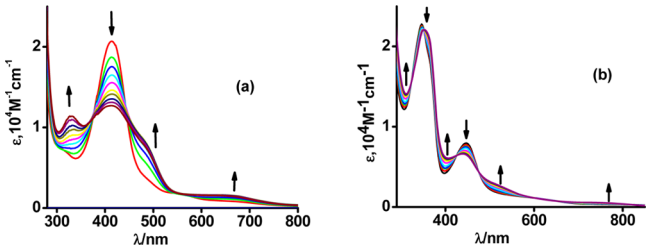

Figure 9. Spectroelectrochemical measurements of (a) **3** and (b) **6** showing the electronic spectra of electrochemically generated 3^+ and 6^+ ions in CH_2Cl_2 at 298 K.

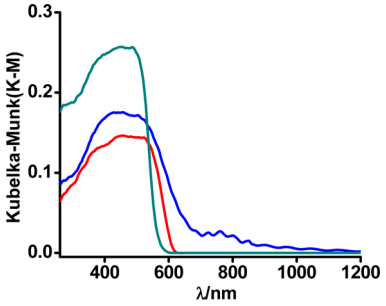

Figure 10. Solid-state UV−vis absorption spectra of **2** (red), **4** (blue), and **7** (green) at 298 K.

Scheme 3

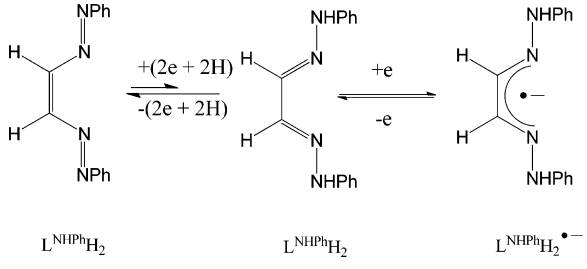

osazone ($L^{NHCONHPh}HMe$) with ruthenium, rhodium, osmium, and iridium ions has been disclosed. $L^{NHPh}H_2$ complexes of osmium(II), *trans*-[$Os^{II}(L^{NHPh}H_2)(PPh_3)_2Br_2$] (**3**), and the phenyl osazone anion radical ($L^{NHPh}H_2^{\bullet-}$) complex of

Scheme 4

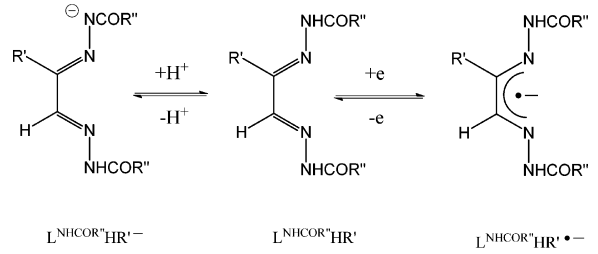

iridium(III), *trans*-[$Ir^{III}(L^{NHPh}H_2^{\bullet-})(PPh_3)_2Cl_2$] (**4**), are reported. Ruthenium(II), osmium(II), and rhodium(III) complexes of neutral benzoyl osazone, benzoyl osazone anion radical ($L^{NHCOPh}H_2^{\bullet-}$), monoanionic tridentate benzoyl osazone ($L^{NCOPh}HMe^-$) ,and neutral tridentate anilido osazone ($L^{NHCONHPh}HMe$) having molecular compositions of the types *trans*-[$Ru^{II}(L^{NHCOPh}H_2)(PPh_3)_2Cl_2$] (**5**), *trans*-[$Os^{II}(L^{NHCOPh}H_2)(PPh_3)_2Br_2$] (**6**), *trans*-[$Rh^{III}(L^{NHCOPh}H_2^{\bullet-})(PPh_3)_2Cl_2$] (**7**), *trans*-[$Rh^{III}(L^{NHCOPh}HMe^-)(PPh_3)_2Cl$]$PF_6$ ([**8**]PF_6), and *trans*-[$Ru^{II}(L^{NHCONHPh}HMe)(PPh_3)_2Cl$]Cl ([**9**]Cl) have been authenticated. The bond parameters of the neutral $L^{NHPh}H_2$, $L^{NHCOPh}H_2$, and $L^{NHCONHPh}HMe$ ligands in **5**, **6**, and $\mathbf{9}^+$ are deformed due to the strong mixing of the metal d orbitals with the π^* orbital of the osazones delocalizing metal electrons to the ligand backbone. This results in a lower M(III)/M(II) reduction potential and low-energy absorption bands, particularly in the osmium analogues **3** and **6**. In the complexes, phenyl osazone is more deformed than the benzoyl osazones. In solids of **2**, **4**, and **7**, spin density is localized on the $L^{NHPh}H_2$ and $L^{NHCOPh}H_2$ ligands, forming anion radical complexes of rhodium(III) and iridium(III) ions as [$M^{III}(L^{NHAr}H_2^{\bullet-})(PPh_3)_2Cl_2$], while in solution the contribution of the nonradical tautomer [$M^{II}(L^{NHAr}H_2)(PPh_3)_2Cl_2$] to the [$M^{III}(L^{NHAr}H_2^{\bullet-})(PPh_3)_2Cl_2$] ↔ [$M^{II}(L^{NHAr}H_2)(PPh_3)_2Cl_2$] equilibria dominates. The irreversible anodic peak potentials of **2**, **4**, and **7** depend significantly on the metal ions. The work infers that the ground state electronic structures of **2**, **4**, and **7** are different in solids and solutions. The conclusion of this work, including the other two reports,[5,6] is that the osazones are redox noninnocent and the redox series

dx.doi.org/10.1021/ic4022432 | Inorg. Chem. 2014, 53, 2427−2440

of the coordinated phenyl osazone are shown in Scheme 3, while the proton transfer and the electron transfer series of benzoyl osazones ($L^{NHCOPh}HR$; R = H, Me) are depicted in Scheme 4.

■ ASSOCIATED CONTENT

Supporting Information

CIF files giving X-ray crystallographic data for **5**, **6**, [**8**]$PF_6 \cdot CH_2Cl_2$, and [**9**]Cl, electronic absorption spectra of $L^{NHPh}H_2$, $L^{NHCOPh}H_2$, $L^{NHCOPh}HMe$, and $L^{NHCONHPh}HMe$ in MeOH at 298 K (Figure S1), electronic absorption spectra of [**9**]Cl in CH_2Cl_2 at 298 K (Figure S2), stretching frequencies (cm^{-1}) of −NH and −C═N− bonds in compounds **1**−**9** (Table S1), excitation energies (λ/nm), oscillator strengths (*f*), significant contributions, transition types, and corresponding MOs of UV/vis/near-IR absorption bands of **3**, $[\mathbf{3}^{Me}]^+$, $[\mathbf{6}^{Me}]^+$, and **7** obtained from TD DFT calculations (Table S2), gas-phase optimized geometries of $L^{Ph}H_2$, $L^{NHPh}H_2$, $L^{NHCOPh}H_2$, $\mathbf{3}^{Me}$, $[\mathbf{3}^{Me}]^+$, $\mathbf{4}^{Me}$, $\mathbf{6}^{Me}$, $[\mathbf{6}^{Me}]^+$, $\mathbf{7}^{Me}$, and $[\mathbf{9}^{Me}]^+$ (Figure S3), selected calculated bond distances and angles of $\mathbf{3}^{Me}$, $\mathbf{4}^{Me}$, and $\mathbf{7}^{Me}$ (Table S3), EPR measurement parameters (Table S4), IR spectra of **3** and electrogenerated $\mathbf{3}^+$ ion (Figure S4), and coordinates of the optimized geometries of $L^{Ph}H_2$, $L^{NHPh}H_2$, $L^{NHCOPh}H_2$, $\mathbf{3}^{Me}$, $[\mathbf{3}^{Me}]^+$, $\mathbf{4}^{Me}$, $\mathbf{6}^{Me}$, $[\mathbf{6}^{Me}]^+$, $\mathbf{7}^{Me}$, and $[\mathbf{9}^{Me}]^+$ (Tables S6−S15). These materials are available free of charge via the Internet at http://pubs.acs.org.

■ AUTHOR INFORMATION

Corresponding Author

*P.G.: e-mail, ghosh@pghosh.in; tel, +91-33-2428-7347; fax, +91-33-2477-3597.

Author Contributions

The manuscript was written through contributions of all authors. All authors have given approval to the final version of the manuscript.

Notes

The authors declare no competing financial interest.

■ ACKNOWLEDGMENTS

Financial support received from the DST (SR/S1/IC/0026/2012) and CSIR 01(2699/12/EMR-II) New Delhi, India is gratefully acknowledged. S.C.P. is grateful to the CSIR (CSIR No.: 08/531(0008)/2013 EMR-I).

■ REFERENCES

(1) (a) Corn, I. R.; Sánchez, P. D. A.; Zdilla, M. J.; Fanwick, P. E.; Shaw, M. J.; Miller, J. T.; Evans, D. H.; Abu-Omar, M. M. *Inorg. Chem.* **2013**, *52*, 5457. (b) Kraft, S. J.; Williams, U. J.; Daly, S. R.; Schelter, E. J.; Kozimor, S. A.; Boland, K. S.; Kikkawa, J. M.; Forrest, W. P.; Christensen, C. N.; Schwarz, D. E.; Fanwick, P. E.; Clark, D. L.; Conradson, S. D.; Bart, S. C. *Inorg. Chem.* **2011**, *50*, 9838. (c) Hartl, F.; Aarnts, M. P.; Nieuwenhuis, H. A.; Slageren, J. V. *Coord. Chem. Rev.* **2002**, *230*, 107.

(2) (a) Lorenz, V.; Hrib, C. G.; Grote, D.; Hilfert, L.; Krasnopolski, M.; Edelmann, F. T. *Organometallics* **2013**, *32*, 4636. (b) Zhou, W.; Chiang, L.; Patrick, B. O.; Storr, T.; Smith, K. M. *Dalton Trans.* **2012**, *41*, 7920. (c) Shaffer, D. W.; Ryken, S. A.; Zarkesh, R. A.; Heyduk, A. F. *Inorg. Chem.* **2011**, *50*, 13. (d) Tsurugi, H.; Saito, T.; Tanahashi, H.; Arnold, J.; Mashima, K. *J. Am. Chem. Soc.* **2011**, *133*, 18673. (e) Khusniyarov, M. M.; Weyhermüller, T.; Bill, E.; Wieghardt, K. *J. Am. Chem. Soc.* **2009**, *131*, 1208 and relevant references therein. (f) Gore-Randall, E.; Irwin, M.; Denning, M. S.; Goicoechea, J. M. *Inorg. Chem.* **2009**, *48*, 8304. (g) Spikes, G. H.; Sproules, S.; Bill, E.; Weyhermüller, T.; Wieghardt, K. *Inorg. Chem.* **2008**, *47*, 10935 and references therein. (h) Bailey, P. J.; Dick, C. M.; Fabre, S.; Parsons, S.; Yellowlees, L. J. *Dalton Trans.* **2006**, 1602. (i) Tuononen, H. M.; Armstrong, A. F. *Dalton Trans.* **2006**, 1885. (j) Tuononen, H. M.; Armstrong, A. F. *Inorg. Chem.* **2005**, *44*, 8277. (k) Baker, R. J.; Farley, R. D.; Jones, C.; Mills, D. P.; Kloth, M.; Murphy, D. M. *Chem. Eur. J.* **2005**, *11*, 2972. (l) Ghosh, P.; Bill, E.; Weyhermuller, T.; Neese, F.; Wieghardt, K. *J. Am. Chem. Soc.* **2003**, *125*, 1293. (m) Pott, T.; Jutzi, P.; Kaim, W.; Schoeller, W. W.; Neumann, B.; Stammler, A.; Stammler, H. G.; Wanner, M. *Organometallics* **2002**, *21*, 3169. (n) Gardiner, M. G.; Hanson, G. R.; Henderson, M. J.; Lee, F. C.; Raston, C. L. *Inorg. Chem.* **1994**, *33*, 2456. (o) Cloke, F. G. N.; Dalby, C. I.; Daff, P. J.; Green, J. C. *J. Chem. Soc., Dalton Trans.* **1991**, 181. (p) Cloke, F. G. N.; Dalby, C. I.; Henderson, M. J.; Hitchcock, P. B.; Kennard, C. H. L.; Lamb, R. N.; Raston, C. L. *J. Chem. Soc. Chem. Commun.* **1990**, 1394 and references therein. (q) Kaim, W.; Ernst, S.; Kasack, V. *J. Am. Chem. Soc.* **1990**, *112*, 173. (r) Kaim, W. *Coord. Chem. Rev.* **1987**, *76*, 187. (s) Creutz, C. *Comments Inorg. Chem.* **1982**, *1*, 293.

(3) (a) Liu, Y.; Yang, P.; Yu, J.; Yang, X.-J.; Zhang, J. D.; Chen, Z.; Schaefer, H. F.; Wu, B. *Organometallics* **2008**, *27*, 5830. (b) Greulich, S.; Stange, A. F.; Stoll, H.; Fiedler, J.; Záliš, S.; Kaim, W. *Inorg. Chem.* **1996**, *35*, 3998.

(4) Gas-phase geometries of $L^{Ph}H_2$, $L^{NHPh}H_2$, and $L^{NHCOPh}H_2$ were optimized with singlet spin stated using the 6-31G basis set to compare the energies of π and π^* orbitals of these ligands. Optimized coordinates are given in Tables S6−S8 (Supporting Information). The calculated energies of HOMO (π) and LUMO (π^*) are as follows: $L^{Ph}H_2$, π = −6.305 eV, π^* = −1.421 eV; $L^{NHPh}H_2$, π = −5.246 eV, π^* = −2.613 eV; $L^{NHCOPh}H_2$, π = −6.002 eV, π^* = −1.82 eV.

(5) Roy, A. S.; Tuononen, H. M.; Rath, S. P.; Ghosh, P. *Inorg. Chem.* **2007**, *46*, 5942.

(6) Patra, S. C.; Biswas, M. K.; Maity, A. N.; Ghosh, P. *Inorg. Chem.* **2011**, *50*, 1331.

(7) (a) Sheldrick, G. M. *ShelXS97*; Universität Göttingen, Göttingen, Germany, 1997. (b) Sheldrick, G. M. *ShelXL97*; Universität Göttingen, Göttingen, Germany, 1997. (c) Platon Program Suite: Spek, A. L. *Acta Crystallogr.* **2009**, *D65*, 148.

(8) Frisch, M. J.; Trucks, G. W.; Schlegel, H. B.; Scuseria, G. E.; Robb, M. A.; Cheeseman, J. R.; Montgomery, J. A.,Jr.; Vreven, T.; Kudin, K. N.; Burant, J. C.; Millam, J. M.; Iyengar, S. S.; Tomasi, J.; Barone, V.; Mennucci, B.; Cossi, M.; Scalmani, G.; Rega, N.; Petersson, G. A.; Nakatsuji, H.; Hada, M.; Ehara, M.; Toyota, K.; Fukuda, R.; Hasegawa, J.; Ishida, M.; Nakajima, T.; Honda, Y.; Kitao, O.; Nakai, H.; Klene, M.; Li, X.; Knox, J. E.; Hratchian, H. P.; Cross, J. B.; Bakken, V.; Adamo, C.; Jaramillo, J.; Gomperts, R.; Stratmann, R. E.; Yazyev, O.; Austin, A. J.; Cammi, R.; Pomelli, C.; Ochterski, J. W.; Ayala, P. Y.; Morokuma, K.; Voth, G. A.; Salvador, P.; Dannenberg, J. J.; Zakrzewski, V. G.; Dapprich, S.; Daniels, A. D.; Strain, M. C.; Farkas, O.; Malick, D. K.; Rabuck, A. D.; Raghavachari, K.; Foresman, J. B.; Ortiz, J. V.; Cui, Q.; Baboul, A. G.; Clifford, S.; Cioslowski, J.; Stefanov, B. B.; Liu, G.; Liashenko, A.; Piskorz, P.; Komaromi, I.; Martin, R. L.; Fox, D. J.; Keith, T.; Al-Laham, M. A.; Peng, C. Y.; Nanayakkara, A.; Challacombe, M.; Gill, P. M. W.; Johnson, B.; Chen, W.; Wong, M. W.; Gonzalez, C.; Pople, J. A. *Gaussian 03, Revision E.01*; Gaussian, Inc., Wallingford, CT, 2004.

(9) (a) *The Challenge of d and f Electrons*; Salahub, D. R., Zerner, M. C., Eds.; American Chemical Society: Washington, DC, 1989. (b) Parr, R. G.; Yang, W. *Density Functional Theory of Atoms and Molecules*; Oxford University Press: Oxford, U.K., 1989. (c) Kohn, W.; Sham, L. J. *Phys. Rev.* **1965**, *140*, A1133. (d) Hohenberg, P.; Kohn, W. *Phys. Rev.* **1964**, *136*, B864.

(10) (a) Stratmann, R. E.; Scuseria, G. E.; Frisch, M. *J. Chem. Phys.* **1998**, *109*, 8218. (b) Casida, M. E.; Jamoroski, C.; Casida, K. C.; Salahub, D. R. *J. Chem. Phys.* **1998**, *108*, 4439. (c) Bauernschmitt, R.; Ahlrichs, R. *Chem. Phys. Lett.* **1996**, *256*, 454.

(11) (a) Becke, A. D. *J. Chem. Phys.* **1993**, *98*, 5648. (b) Miehlich, B.; Savin, A.; Stoll, H.; Preuss, H. *Chem. Phys. Lett.* **1989**, *157*, 200. (c) Lee, C.; Yang, W.; Parr, R. G. *Phys. Rev. B* **1988**, *37*, 785.

(12) Pulay, P. *J. Comput. Chem.* **1982**, *3*, 556.

(13) Schlegel, H. B.; McDouall, J. J. In *Computational Advances in Organic Chemistry*; Ogretir, C., Csizmadia, I. G., Eds.; Kluwer Academic: Dordrecht, The Netherlands, 1991; p 167.
(14) Hay, P. J.; Wadt, W. R. *J. Chem. Phys.* **1985**, *82*, 270.
(15) Wadt, W. R.; Hay, P. J. *J. Chem. Phys.* **1985**, *82*, 284.
(16) Hay, P. J.; Wadt, W. R. *J. Chem. Phys.* **1985**, *82*, 299.
(17) (a) Rassolov, V. A.; Ratner, M. A.; Pople, J. A.; Redfern, P. C.; Curtiss, L. A. *J. Comput. Chem.* **2001**, *22*, 976. (b) Francl, M. M.; Pietro, W. J.; Hehre, W. J.; Binkley, J. S.; DeFrees, D. J.; Pople, J. A.; Gordon, M. S. *J. Chem. Phys.* **1982**, *77*, 3654. (c) Hariharan, P. C.; Pople, J. A. *Mol. Phys.* **1974**, *27*, 209. (d) Hariharan, P. C.; Pople, J. A. *Theo. Chim. Acta* **1973**, *28*, 213. (e) Hehre, W. J.; Ditchfield, R.; Pople, J. A. *J. Chem. Phy.* **1972**, *56*, 2257.
(18) (a) Rassolov, V.; Pople, J. A.; Ratner, M.; Windus, T. L. *J. Chem. Phys.* **1998**, *109*, 1223. (b) Francl, M. M.; Petro, W. J.; Hehre, W. J.; Binkley, J. S.; Gordon, M. S.; DeFrees, D. J.; Pople, J. A. *J. Chem. Phys.* **1982**, *77*, 3654. (c) Hariharan, P. C.; Pople, J. A. *Theor. Chim. Acta* **1973**, *28*, 213.
(19) (a) Gordon, M. S.; Binkley, J. S.; Pople, J. A.; Pietro, W. J.; Hehre, W. J. *J. Am. Chem. Soc.* **1983**, *104*, 2797. (b) Binkley, J. S.; Pople, J. A.; Hehre, W. J. *J. Am. Chem. Soc.* **1980**, *102*, 939.
(20) O'Boyle, N. M.; Tenderholt, A. L.; Langner, K. M. *J. Comput. Chem.* **2008**, *29*, 839.
(21) (a) Cossi, M.; Rega, N.; Scalmani, G.; Barone, V. *J. Comput. Chem.* **2003**, *24*, 669. (b) Barone, V.; Cossi, M. *J. Phys. Chem. A* **1998**, *102*, 1995.
(22) (a) Biswas, M. K.; Patra, S. C.; Maity, A. N.; Ke, S.-C.; Adhikary, N. D.; Ghosh, P. *Inorg. Chem.* **2012**, *51*, 6687. (b) Hsu, F. C.; Tung, Y. L.; Chi, Y.; Hsu, C. C.; Cheng, Y. M.; Ho, M. L.; Chou, P. T.; Peng, S. M.; Carty, A. J. *Inorg. Chem.* **2006**, *45*, 10188. (c) Acharyya, R.; Dutta, S.; Basuli, F.; Peng, S.-M.; Lee, G.-H.; Falvello, L. R.; Bhattacharya, S. *Inorg. Chem.* **2006**, *45*, 1252 and references therein. (d) Ghosh, P.; Bag, N.; Chakravorty, A. *Organometallics* **1996**, *15*, 3042.
(23) Representative current references of the X-ray structures of the complexes in which residual electron density near the heavier transition-metal ions is comparatively higher and spans a range of 3.2−11.384 e $Å^{-3}$: (a) Almodares, Z.; Lucas, S. J.; Crossley, B. D.; Basri, A. M.; Pask, C. M.; Hebden, A. J.; Phillips, R. M.; McGowan, P. C. *Inorg. Chem.* **2014**, *53*, 727. (b) Pellegrino, J.; Gaviglio, C.; Milstein, D.; Doctorovich, F. *Organometallics* **2013**, *32*, 6555. (c) Sommer, M. G.; Schweinfurth, D.; Weisser, F.; Hohloch, S.; Sarkar, B. *Organometallics* **2013**, *32*, 2069. (d) Deibel, N.; Hohloch, S.; Sommer, M. G.; Schweinfurth, D.; Ehret, F.; Braunstein, P.; Sarkar, B. *Organometallics* **2013**, *32*, 7366. (e) Nakajima, T.; Kurai, S.; Noda, S.; Zouda, M.; Kure, B.; Tanase, T. *Organometallics* **2012**, *31*, 4283. (f) Cowie, B. E.; Emslie, D. J. H.; Jenkins, H. A.; Britten, J. F. *Inorg. Chem.* **2010**, *49*, 4060. (g) Mirtschin, S.; Krasniqi, E.; Scopelliti, R.; Severin, K. *Inorg. Chem.* **2008**, *47*, 6375. (h) Aguirre, J. D.; Lutterman, D. A.; Angeles-Boza, A. M.; Dunbar, K. R.; Turro, C. *Inorg. Chem.* **2007**, *46*, 7494. (i) Sekioka, Y.; Kaizaki, S.; Mayer, J. M.; Suzuki, T. *Inorg. Chem.* **2005**, *44*, 8173.
(24) (a) Biswas, M. K.; Patra, S. C.; Maity, A. N.; Ke, S.-C.; Weyhermüller, T.; Ghosh, P. *Dalton Trans.* **2013**, *42*, 6538. (b) Das, A.; Basuli, F.; Peng, S.-M.; Bhattacharya, S. *Inorg. Chem.* **2002**, *41*, 440. (c) Dutta, S.; Peng, S.-M.; Bhattacharya, S. *J. Chem. Soc., Dalton Trans.* **2000**, 4623. (d) Pattanayak, S.; Chattopadhyay, S.; Ghosh, K.; Ganguly, S.; Ghosh, P.; Chakravorty, A. *Organometallics* **1999**, *18*, 1486.
(25) (a) Hetterscheid, D. G. H.; Klop, M.; Kicken, R. J. N. A. M.; Smits, J. M. M.; Reijerse, E. J.; de Bruin, B. *Chem. Eur. J.* **2007**, *13*, 3386. (b) Menglet, D.; Bond, A. M.; Coutinho, K.; Dickson, R. S.; Lazarev, G. G.; Olsen, S. A.; Pilbrow, J. R. *J. Am. Chem. Soc.* **1998**, *120*, 2086.
(26) Kubelka, P.; Munk, F. *Z. Tech. Phys.* **1931**, *12*, 593.

dx.doi.org/10.1021/ic4022432 | *Inorg. Chem.* 2014, 53, 2427−2440